Cell Reports

Article

A Dynamic Splicing Program Ensures Proper Synaptic Connections in the Developing Cerebellum

Graphical Abstract

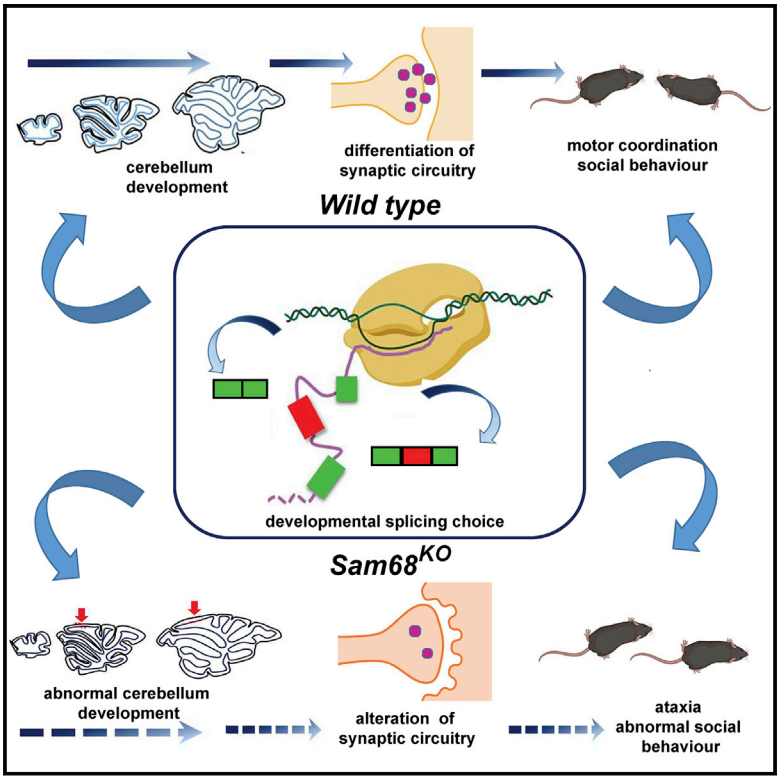

Authors

Donatella Farini, Eleonora Cesari, Robert J. Weatheritt, ..., Benjamin J. Blencowe, Daniela Marazziti, Claudio Sette

Correspondence

claudio.sette@unicatt.it

In Brief

Alternative splicing contributes to all steps of brain development. Farini et al. show that maturation of the cerebellum involves a dynamic splicing program that mainly affects synaptic genes. Precocious dysregulation of this program by Sam68 ablation alters cerebellar neuronal connectivity and results in defective motor coordination and social behavior.

Highlights

- A dynamic splicing program shapes the cerebellar transcriptome during development
- Autism-spectrum-disorder-related genes exhibit developmental splicing regulation
- Sam68 establishes a splicing signature that ensures proper synaptic maturation
- Sam68 regulates genes associated with autism spectrum disorder and social behavior

Farini et al., 2020, Cell Reports *31*, 107703
June 2, 2020 © 2020 The Author(s).
https://doi.org/10.1016/j.celrep.2020.107703

CellPress

Cell Reports

CellPress
OPEN ACCESS

Article

A Dynamic Splicing Program Ensures Proper Synaptic Connections in the Developing Cerebellum

Donatella Farini,[1,2] Eleonora Cesari,[3,4] Robert J. Weatheritt,[5,6] Gina La Sala,[7] Chiara Naro,[3,4] Vittoria Pagliarini,[3,4] Davide Bonvissuto,[3] Vanessa Medici,[1,2] Marika Guerra,[3,4] Chiara Di Pietro,[7] Francesca Romana Rizzo,[8,9] Alessandra Musella,[9] Valeria Carola,[2,10] Diego Centonze,[8,11] Benjamin J. Blencowe,[5] Daniela Marazziti,[7] and Claudio Sette[2,3,12,*]

[1]Department of Biomedicine and Prevention, University of Rome Tor Vergata, Rome, Italy
[2]Fondazione Santa Lucia, IRCCS, Rome, Italy
[3]Department of Neuroscience, Section of Human Anatomy, Catholic University of the Sacred Heart, Rome, Italy
[4]Fondazione Policlinico Universitario A. Gemelli, IRCCS, Rome, Italy
[5]Donnelly Centre and Department of Molecular Genetics, University of Toronto, Toronto, ON, Canada
[6]EMBL Australia, Garvan Institute of Medical Research, Darlinghurst, NSW, Australia
[7]Institute of Cell Biology and Neurobiology, CNR, Monterotondo, Rome, Italy
[8]Department of Systems Medicine, University of Rome Tor Vergata, Rome, Italy
[9]San Raffaele Pisana and University San Raffaele, IRCCS, Rome, Italy
[10]Department of Dynamic and Clinical Psychology, University of Rome Sapienza, Rome, Italy
[11]Unit of Neurology, IRCCS Neuromed, Pozzilli, Isernia, Italy
[12]Lead Contact
*Correspondence: claudio.sette@unicatt.it
https://doi.org/10.1016/j.celrep.2020.107703

SUMMARY

Tight coordination of gene expression in the developing cerebellum is crucial for establishment of neuronal circuits governing motor and cognitive function. However, transcriptional changes alone do not explain all of the switches underlying neuronal differentiation. Here we unveiled a widespread and highly dynamic splicing program that affects synaptic genes in cerebellar neurons. The motifs enriched in modulated exons implicated the splicing factor Sam68 as a regulator of this program. Sam68 controls splicing of exons with weak branchpoints by directly binding near the 3′ splice site and competing with U2AF recruitment. Ablation of Sam68 disrupts splicing regulation of synaptic genes associated with neurodevelopmental diseases and impairs synaptic connections and firing of Purkinje cells, resulting in motor coordination defects, ataxia, and abnormal social behavior. These findings uncover an unexpectedly dynamic splicing regulatory network that shapes the synapse in early life and establishes motor and cognitive circuitry in the developing cerebellum.

INTRODUCTION

The mammalian cerebellum controls motor and non-motor behaviors and has a relatively simple architecture comprising deep nuclei and an extremely dense cortical region. The cerebellar cortex is organized in three layers: the molecular layer (ML), the Purkinje cell (PC) layer (PL), and the inner granular layer (IGL), which are folded to form lobules (Sillitoe and Joyner, 2007). PCs are GABAergic inhibitory neurons and represent the only output of the cerebellar cortex. They receive excitatory signals by the parallel fibers of glutamatergic granule cells (GCs), the most abundant neuronal population in the brain, and by climbing fibers from the inferior olive (Sillitoe and Joyner, 2007). PC axons converge on neurons of deep nuclei and control their firing. Because deep cerebellar nuclei establish extensive connections with multiple areas of the cerebral cortex, disruption of the cerebellar circuitry, especially during critical periods of development, contributes to neurodevelopmental disorders characterized by motor, sensitive, and cognitive deficits (Sathyanesan et al., 2019; Wang et al., 2014).

Cerebellum development in mice occurs in a prolonged window ranging from embryonic day 9 (E9) to the third postnatal week. After rounds of proliferation in the external granular layer (EGL), postmitotic GCs migrate radially through the ML and the PCL. During their journey to reach the IGL, GCs connect with mossy fibers, which are glutamatergic afferents from spinal cord nuclei, and project axons that grow as parallel fibers and synapse with the developing PC dendritic tree (Sillitoe and Joyner, 2007). Inward accumulation of the GCs, their change in shape, and their migration through the ML contribute to mold the fissures between lobules (Legué et al., 2016). Conversely, defective maturation or migration of GCs results in abnormal cerebellar morphogenesis with disrupted spatial organization of lobules and impaired cerebellar circuitry (Sathyanesan et al., 2019; Wang et al., 2014).

Fine-tuned transcriptional programs orchestrate the sequential steps of cerebellar development (Sillitoe and Joyner, 2007) by synchronizing differentiation of PCs and promoting migration of GCs (Rodriques et al., 2019; Rosenberg et al., 2018). Alternative splicing (AS) is another key step of gene expression

This is an open access article under the CC BY-NC-ND license (http://creativecommons.org/licenses/by-nc-nd/4.0/).

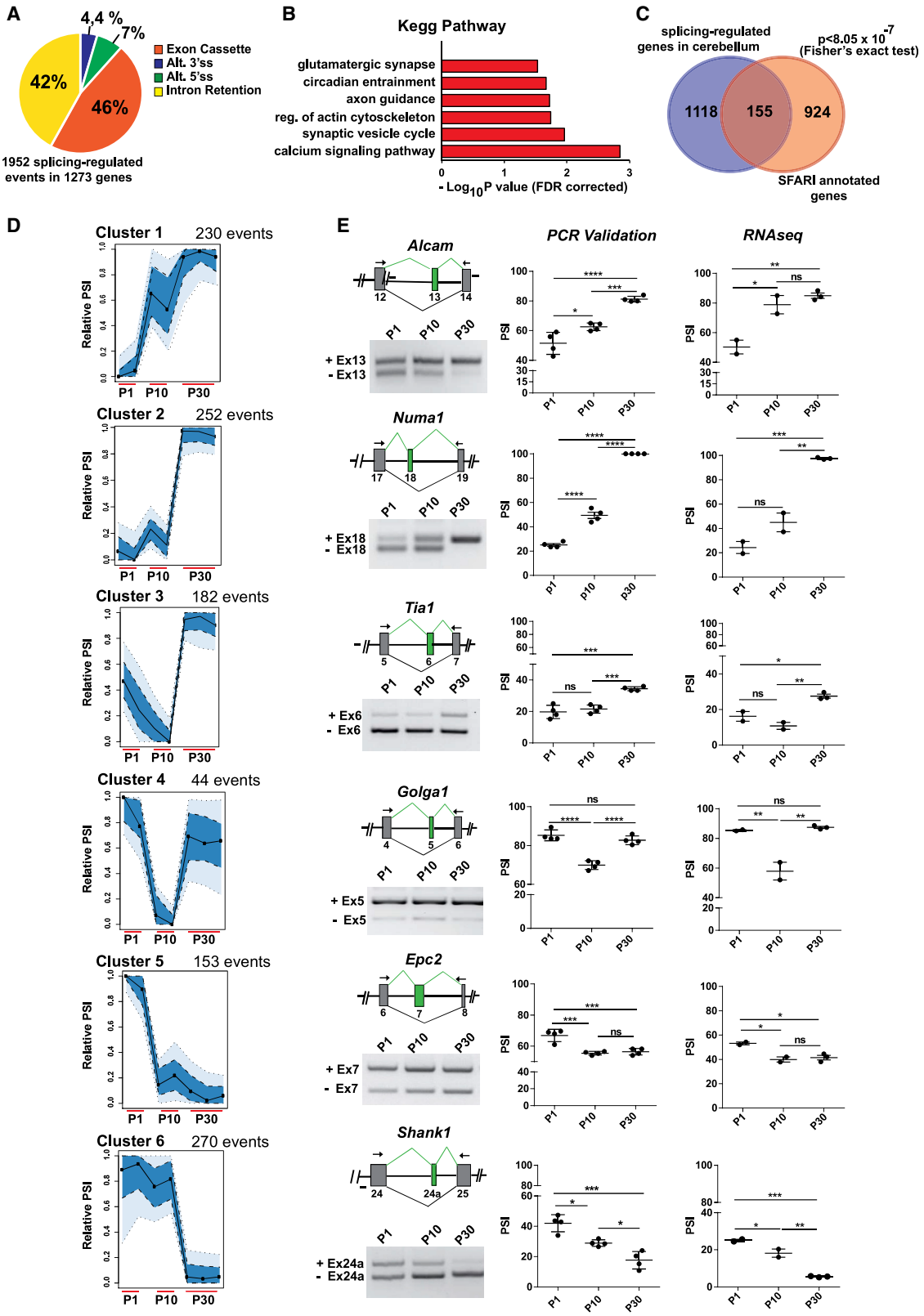

(legend on next page)

regulation that is tightly modulated in the brain (Raj and Blencowe, 2015; Vuong et al., 2016). Splicing consists of removal of introns and ligation of adjacent exons in precursor mRNA (pre-mRNA) and is operated by the spliceosome, a complex machinery comprising five small nuclear ribonucleoproteins (U1, U2, U4, U5, and U6 small nuclear ribonucleoprotein particles [snRNPs]) and hundreds of auxiliary proteins (Fu and Ares, 2014). Because the heterogeneity of splice site sequences at exon-intron junctions diminishes the ability of the spliceosome to unequivocally recognize them, spliceosome assembly requires cooperation of sequence-specific splicing factors that bind additional sites in the pre-mRNA. Competition between antagonistic splicing factors yields AS events in virtually all mammalian genes (Fu and Ares, 2014), greatly expanding the coding potential and flexibility of the genome. Temporal and spatial regulation of splice variants is required for all steps of neural development, from neurogenesis and neuronal migration (La Rosa et al., 2016; Zhang et al., 2016) to synaptic function and behavior (Ehrmann et al., 2016; Traunmüller et al., 2016). Splice variants of the same gene can yield synaptic proteins with different functions. For instance, AS of presynaptic voltage-gated calcium channels affects their affinity for intracellular partners and interaction with synaptic vesicles, modulating short-term plasticity (Heck et al., 2019). Likewise, AS of a single exon in presynaptic neurexin proteins dictates the choice between postsynaptic N-methyl-D-aspartate (NMDA) or α-amino-3-hydroxy-5-methyl-4-isoxazolepropionic acid (AMPA) receptors, in turn affecting synaptic responses (Dai et al., 2019). Thus, splicing modulation elicits direct control of cerebral circuitry by influencing synapse formation, integrity, and function.

Here we uncovered a highly dynamic splicing program that accompanies cerebellar development and particularly affects genes encoding synaptic proteins involved in human neurodevelopmental disorders. This program is extensively modulated by the splicing factor Sam68, whose ablation resulted in impaired development, permanent defects of glutamatergic synaptic function, and abnormal motor and social behavior. Thus, our findings point to splicing regulation as a key developmental mechanism that warrants establishment of proper motor and cognitive circuitry in the cerebellum.

RESULTS

Cerebellar Development Involves Extensive AS Switches

To evaluate the effect of splicing regulation on the cerebellar transcriptome, we performed high-throughput RNA sequencing (RNA-seq) analyses at key stages of development. At postnatal day 1 (P1), PCs start to mature, whereas GCs proliferate in the EGL. At P10, post-mitotic GCs migrate to populate the IGL. At P30, cerebellar differentiation is complete, and neurons have acquired mature synaptic function (Sillitoe and Joyner, 2007; Legué et al., 2016). Comparison of gene expression levels confirmed robust transcriptional changes during cerebellar development with involvement of 1,317 genes (reads per kilobase million [cRPKM] values, false discovery rate [FDR] < 0.05, 10.2% of expressed genes; Table S1). Furthermore, profiling of AS events by using the Vertebrate Alternative Splicing and Transcription Tools (Vast-Tools) pipeline (https://github.com/vastgroup/vast-tools) uncovered activation of a widespread splicing program with 1,952 events in 1,273 genes that were modulated during development (Figure 1A). Genes modulated at the expression and splicing levels were enriched in similar functional categories related to nervous system development and synaptogenesis. However, the overlap was limited (<20%) (Figures S1A and S1B), suggesting that concomitant activation of gene expression and splicing programs contributes to remodel the transcriptome during cerebellar development.

The majority of AS events affected during development belonged to the cassette exon and intron retention (IR) categories (Figure 1A; Table S1). AS-regulated genes were significantly enriched in functional categories related to Ca^{2+} signaling, cytoskeleton, and glutamatergic synapses (Figure 1B). Analysis of an independent RNA-seq dataset of the developing cerebellum (Pal et al., 2011; GSE23525) revealed that 72.7% (32 of 44) of the AS events were regulated in the same direction (Figures S1C and S1D; $p = 2.85 \times 10^{-04}$, Fisher's exact test), indicating reproducible detection of these splicing changes. Moreover, comparison with splicing changes in the human cerebellum at different ages (Mazin et al., 2013) showed a remarkably high level (72.0%, 170 of 236) of conservation (Figures S1E and S1F; $p = 1.26 \times 10^{-41}$, Fisher's exact test).

Altered cerebellar development is a strong risk factor for autism spectrum disorder (ASD) (Sathyanesan et al., 2019; Wang et al., 2014). Thus, we asked whether splicing-regulated genes were associated with this neurodevelopmental syndrome. Indeed, 155 splicing-modulated genes are associated with ASD (https://gene.sfari.org; Figure 1C; $p < 8.05 \times 10^{-07}$, Fisher's exact test; Table S1), suggesting a potential link between splicing regulation in the cerebellum and this disease.

Analysis through a machine learning approach (self-organized maps) identified six different splicing regulatory patterns (Figure 1D). Profiling of exons for their inclusion (percent spliced in [PSI]) levels showed that most alternative exons were either

Figure 1. An Extensive AS Program Characterizes Development of the Mouse Cerebellum

(A) Pie chart showing the percentage of AS events regulated in the cerebellum at P1, P10, and P30.

(B) KEGG (Kyoto Encyclopedia of Genes and Genomes) functional annotation of AS-modulated genes.

(C) Overlap of splicing-regulated genes in the cerebellum and ASD-linked genes (Simons Foundation Autism Research Initiative [SFARI] database). Population of expressed genes in cerebellum = 12,130.

(D) Clustering of the developmentally regulated exon cassette and alternative 3′ and 5′ splice sites. Polygon plots show the median values as a black line. Dark blue represents the 0.25–0.75 quantiles and light blue 0.1–0.9 percentiles.

(E) RT-PCR analyses of one event for each cluster (left panels); black arrows in the scheme of the event indicate PCR primers. The center panels show graphs of PSI levels from RT-PCR analysis. Mean ± SEM, n = 4; one-way ANOVA, Tukey's multiple comparisons test; ns, not significant; *p < 0.05; **p < 0.01; ***p < 0.001; ****p < 0.0001. The right panels show PSI values from RNA-seq.

See also Figures S1 and S2 and Table S1.

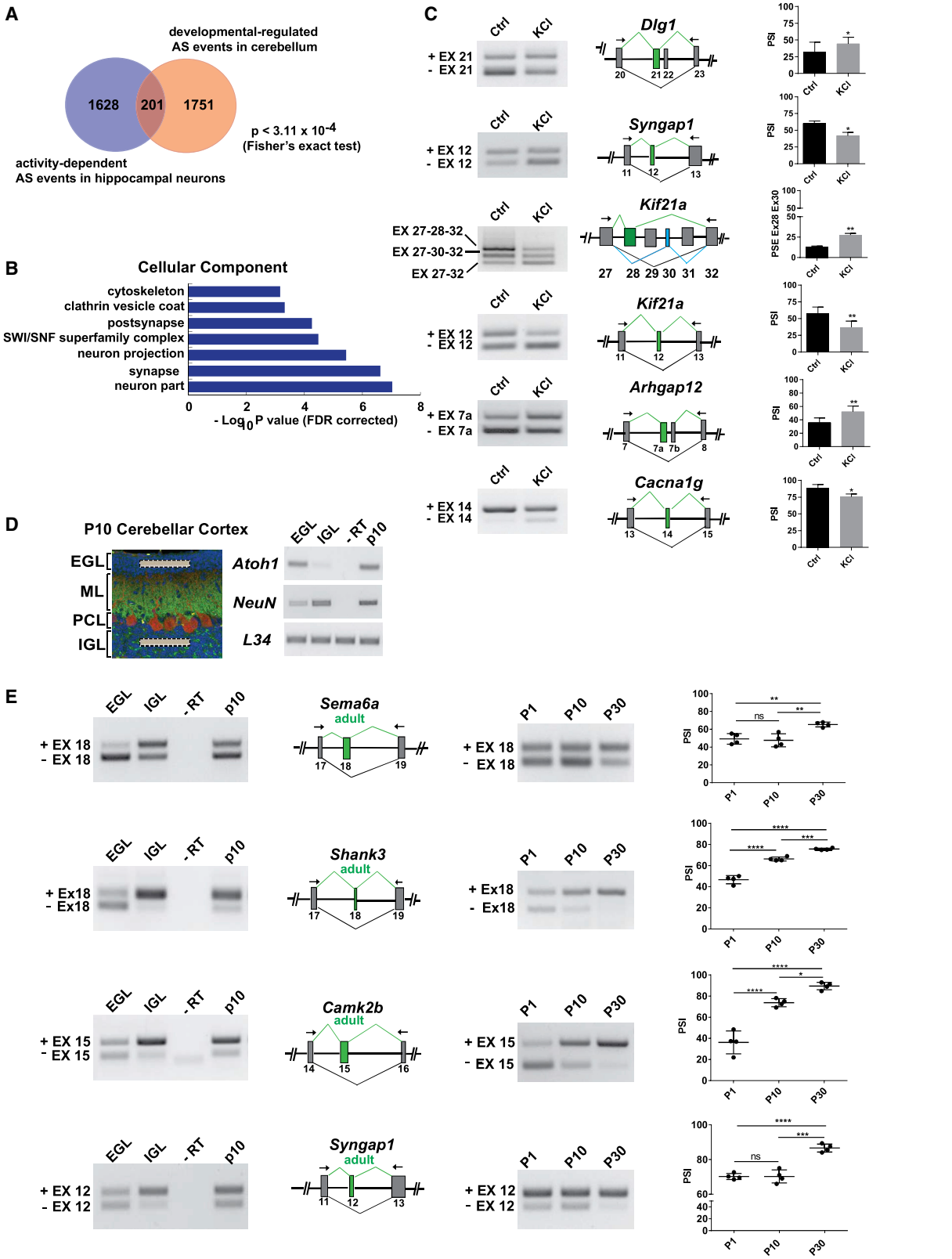

(legend on next page)

progressively included (clusters 1 and 2, maximal PSI at P30) or skipped (clusters 5 and 6, maximal PSI at P1) during development (Figure 1D; Table S1). However, other exons displayed a dynamic regulation with transient skipping at P10 (clusters 3 and 4), when GCs migrate and functional synaptic connections are being established. Similar organization in temporal clusters was observed for IR events (Figure S2A; Table S1), which were also enriched in genes involved in synapse and neurite structure (Figure S2B). Inspection of randomly chosen events yielded a more than 80% validation rate (31 of 38) (Figures 1E, 2E, 4F, S2A, and S3C). These results reveal activation of a highly dynamic splicing program during cerebellar development.

The Cerebellar Splicing Program Is Activity-Regulated and Spatially Regulated during Development

Activity-dependent signaling networks can regulate synapse development and plasticity by modulating AS of genes encoding synaptic proteins (Iijima et al., 2011; Quesnel-Vallières et al., 2016). Importantly, this activity-dependent program is dysregulated in ASD (Quesnel-Vallières et al., 2016, 2019). Thus, we asked whether changes in AS during cerebellar development might be related, at least in part, to activity-dependent pathways. Comparison of developmentally regulated AS events in the cerebellum (Figure 1A) with those regulated by depolarization of hippocampal neurons (Quesnel-Vallières et al., 2016) highlighted 201 exons in common (Figure 2A; $p < 3.11 \times 10^{-4}$, Fisher's exact test), most of which (74%) were cassette exon events (Table S2). Analysis of another dataset from cortical mouse neurons undergoing depolarization (Maze et al., 2015) yielded comparable results (Figure S3A; Table S2). Cellular component analysis showed that the cerebellar depolarization-dependent, splicing-regulated genes were primarily related to synapse function and the cytoskeleton (Figure 2B).

GCs represent the vast majority of cells in the cerebellum (Sillitoe and Joyner, 2007). Thus, to test whether these exons were modulated by GC depolarization, we cultured them for 10 days *in vitro* (DIV), when they were competent for activation (Figure S3B). Depolarization of GCs caused AS regulation of two synaptic genes identified by the overlap analysis (*Dlg1* and *Syngap1*) (Figure 2C). Moreover, additional developmentally regulated exons of synaptic genes (*Kif21a*, *Arhgap12*, and *Cacna1g*), which were not included in the overlap, were also regulated by depolarization (Figure 2C). These results suggest that developmentally regulated exons in synaptic genes are sensitive to GC activation.

A key feature of postnatal cerebellar development is represented by migration of GCs. Because developmentally regulated AS events were enriched in genes involved in cytoskeleton organization and morphogenesis (Figure 1B), we hypothesized that their regulation could correlate with or be functional for migration and differentiation of GCs. To test whether splice variants of these genes were subjected to spatial regulation, we separated the EGL and IGL of P10 cortex by laser-capture microdissection (Figure 2D). Analysis of genes involved in migration (*Sema6a*) (Kerjan et al., 2005) and actin cytoskeleton and dendritic spine morphogenesis (*Shank3*, *Camk2b*, and *Syngap1*) (Jeyabalan and Clement, 2016; Roussignol et al., 2005; Sugawara et al., 2017) showed region-specific regulation (Figure 2E, left panels). The spatial switch in splice variants from the EGL to the IGL recapitulated that observed in the total cerebellum from P10 to P30 (Figures 2E and S3C). Moreover, GCs also acquired the mature splicing pattern when cultured *in vitro* for 5–10 days, indicating that this process is cell autonomous (Figure S3D). These results suggest that developmentally regulated splice variants may play a role in GC migration and maturation.

Sam68 Modulates a Dynamic Splicing Program during Cerebellar Development

To identify factors involved in control of the cerebellar splicing program, we searched for sequence motifs recognized by RNA binding proteins (Ray et al., 2013). Bioinformatics analysis using the rMAPs tool (http://rmaps.cecsresearch.org/) indicated that, with the exception of cluster 1, binding motifs for the STAR (signal transduction and activation of RNA) proteins KHDRBS1 (Sam68), KHDRBS2 (Slm1), and KHDRBS3 (Slm2) were enriched in regulated exons and neighboring introns (Figure 3A; Table S3). We also found enrichment in motifs for neuron-specific splicing factors (Raj and Blencowe, 2015), such as ELAV2/4, BRUNOL6, nSR100, NOVA1, and RBFOX2/3, but they were generally limited to fewer clusters (Figure 3A).

The KHDRBS1–KHDRBS3 proteins are highly homologous, have very similar binding motifs (Figure 3B), and function similarly in splicing regulation (Ehrmann et al., 2016; Feracci et al., 2016; Danilenko et al., 2017). Real-time qPCR analyses showed that *Khdrbs1* was always the most expressed gene in the cerebellum, whereas *Khdrbs2* and *Khdrbs3* transcripts were barely detected (Figure 3C). Thus, we focused on KHDRBS1/Sam68 (hereafter referred to as Sam68).

RNA-seq analysis of *Sam68* wild-type (WT) and knockout ($Sam68^{KO}$) cerebella identified 350 AS events that were

Figure 2. Developmentally Modulated Splicing Events Are Sensitive to Neuron Depolarization and Spatial Distribution in the Developing Cerebellum

(A) Overlap between AS events regulated by neuronal activation (blue, GSE89984) and cerebellar development (orange, this study; GSE133711.

(B) Cellular component annotation for overlapping genes.

(C) AS changes induced by depolarization of cerebellar GCs with 25 mM KCl for 3 h. Left panels: RT-PCR analysis of AS events schematized in the center panels. Right panels: PSI levels from RT-PCR analysis of GCs (for *Kif21a* percent splicing exclusion [PSE] of exon 28 [Ex28] and Ex30). Mean ± SEM, n = 3; two-tailed paired t test; *p < 0.05, **p < 0.01.

(D) Left panel: P10 cerebellar cortex image with laser-dissected regions (gray boxes). Right panel: enrichment of EGL (*Atoh1*) and IGL (*NeuN*) markers in laser-captured regions.

(E) Left panel: RT-PCR analysis of AS events in the EGL and IGL regions. IGL RNA without reverse transcriptase (−RT) was used as a negative control. Right panels: RT-PCR analysis of the same AS events analyzed at different ages. Graphs show PSI levels from RT-PCR analysis at the indicated ages. Mean ± SEM, n = 4; one-way ANOVA, Tukey's multiple comparisons test; *p < 0.05, **p < 0.01, ***p < 0.001, ****p < 0.0001.

See also Figure S3 and Table S2.

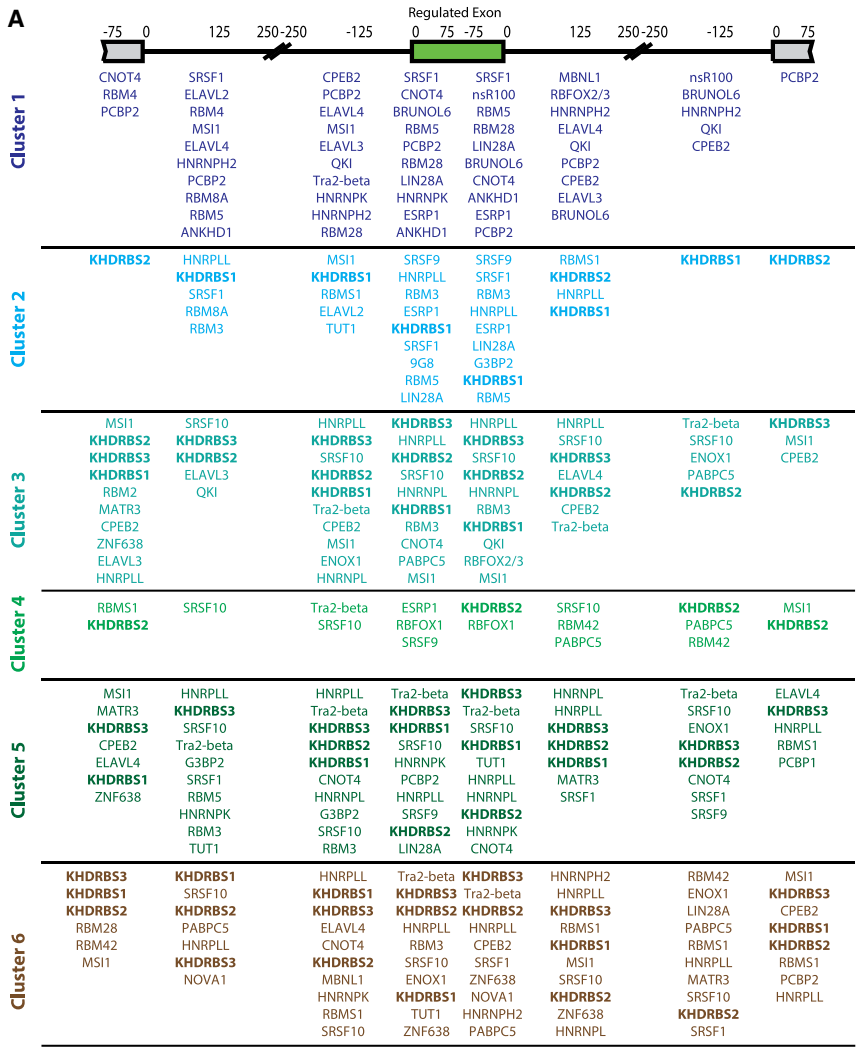

Figure 3. Developmentally Regulated Exons Are Enriched in Consensus Motifs for Sam68, Slm1, and Slm2

(A) RNA-binding proteins (RBPs) predicted to bind *cis*-acting elements enriched in regulated cassette exons and adjacent regions for each developmental cluster. Enriched motifs ($p < 0.01$) were identified using the computational tool in the rMAPS web server. The 10 RBPs displaying the most significantly enriched motif are shown for each cluster, top-down according to increasing p value.

(B) Consensus motifs for KHDRBS1 (Sam68), KHDRBS2 (Slm1), and KHDRBS3 (Slm2) from rMAPS analysis.

(C) qPCR analysis of STAR protein expression in the cerebellum.

See also Table S3.

susceptible to Sam68 ablation at P1 and 384 events at P10 (Figures 4A and 4B; Table S4). In contrast, no gene besides *Sam68* itself was affected at expression level in the *Sam68*^{KO} cerebellum (Figures S4A and S4B). Sam68-regulated splicing events were enriched in genes involved synaptic functions (Figure S4C). Moreover, gene ontology analysis using the Enrichr database (http://amp.pharm.mssm.edu/Enrichr) identified abnormal synaptic transmission and spinocerebellar ataxia as, respectively, the most significant mammalian phenotype and human disease associated with Sam68 target genes (Figures S4D and S4E). These observations supported a potential role of Sam68 in establishment of cerebellar circuits.

The cassette exon is the most abundant splicing pattern regulated by Sam68 in the cerebellum (Figures 4A and 4B), followed by IR. The majority of these events were upregulated in the knockout cerebellum (Figures 4A and 4B), indicating that Sam68 generally represses exon recognition, whereas it is required for proper splicing of target introns. Exons that have been shown previously to be regulated by Sam68 in other systems (i.e., exon 19 in *Nrxn1*, exon 24 in *Stxbp5l*, exon 28 in *Kif21a*, and exon 9 in *Sgce*; Ehrmann et al., 2016; Iijima et al., 2011; Paronetto et al., 2011) were included in our dataset (Table S4). Further analysis of Sam68-regulated events yielded a validation rate of more than 70% (Figures S4F and 5A–5C). These results highlight a widespread effect of Sam68 on splicing regulation in the cerebellum.

Comparison of developmentally regulated events with those sensitive to Sam68 expression showed a highly significant overlap (Figures 4C and 4D; $p = 2.7 \times 10^{-89}$, Fisher's exact test). Furthermore, Sam68-regulated splicing events were enriched in genes linked to ASD (Figure 4E; $p = 2.08 \times 10^{-7}$, Fisher's exact test) but not to other neurological diseases, such as schizophrenia ($p < 0.44$, Fisher's exact test) or bipolar disorder ($p < 0.86$, Fisher's exact test) (Figures S5D and S5E). Inspection of the Vastdb database revealed that 30.8% of the Sam68-regulated events for which information is available (42

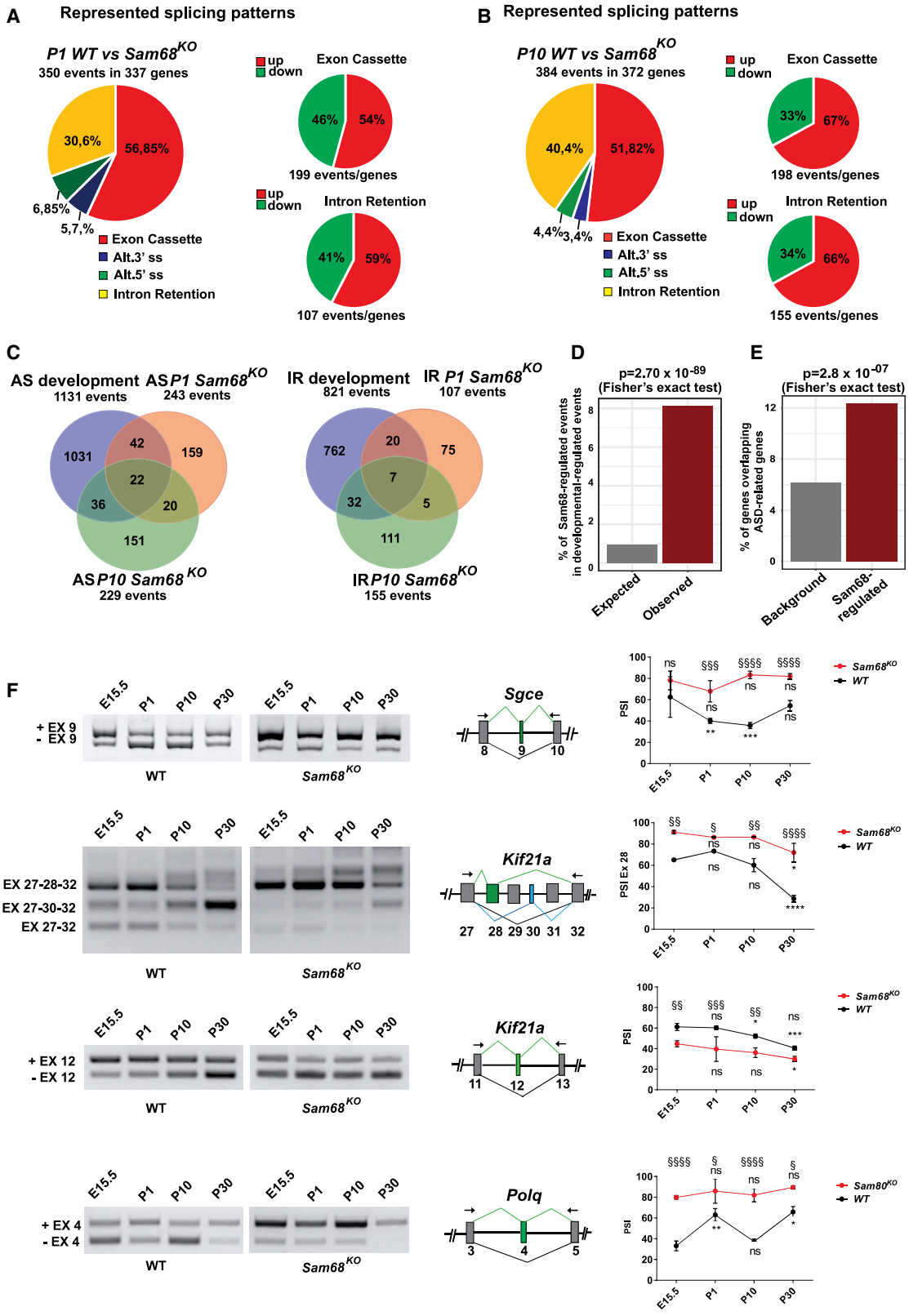

(legend on next page)

of 130) caused alteration of the open reading frame (ORF), either by introducing a premature stop codon or by causing a frameshift, indicating the functional effect on the corresponding proteins. Among them, we found key genes involved in glutamatergic synapses, such as *Gria2* (*glutamate ionotropic receptor AMPA type subunit* 2) and *Gria3*, which encode subunits of the glutamate receptor. Knockout of *Sam68* caused retention of intron 11 in *Gria2* and of intron 12 in *Gria3*, events that likely yield premature termination of the transcript by cleavage and alternative polyadenylation at cryptic sites annotated in these introns (Figure S5C). In support of this hypothesis, we observed reduced levels of GRIA2 protein in *Sam68*^{KO} cerebellar extract (Figure S5F). Remarkably, analysis of four developmentally regulated exons in the *Sgce*, *Kif21a* (exon 12 and 28), and *Polq* genes in a time frame from E15.5 to P30 showed highly dynamic splicing patterns that were almost completely ablated in the absence of Sam68 (Figure 4F). These findings uncover a key role of Sam68 in execution of the developmental splicing program in the cerebellum.

Sam68 Competes with the U2AF Complex to Repress Exons with Weak Branchpoints

To gain insights into the mechanism by which Sam68 modulates splicing, we searched for sequence features associated with the regulated exons. No significant differences were found in the strength of splice sites or in intron or exon length (Figures S6A–S6D). However, the branchpoint sequence of Sam68-regulated exons was significantly weaker than that of non-regulated exons ($p < 4.94 \times 10^{-05}$; Figure S6E). Furthermore, analysis of exons that were up- or downregulated in the *Sam68*^{KO} cerebellum clearly indicated that the weaker branchpoint was a feature of upregulated exons ($p < 4.74 \times 10^{-08}$; Figure 5A). Upregulated exons also displayed lower GC content (Figure 5B), a feature recently linked to exons characterized by higher variability in branchpoint sequences (Lemaire et al., 2019), whereas downregulated exons displayed higher GC content (Figure 5B). Moreover, the ΔPSI (the difference in PSI between *Sam68*^{KO} and the WT) distribution indicated that the effect of Sam68 ablation was stronger for upregulated exons (higher ΔPSI, $p < 0.001$; Figure 5C). Together with evidence showing that the majority of Sam68-target exons are upregulated in the knockout cerebellum (Figures 4A and 4B), these findings suggest that Sam68 prevalently represses exons characterized by a weak branchpoint and low GC content.

The branchpoint region is recognized by the U2 snRNP, whose recruitment is favored by binding of the U2AF complex to the polypyrimidine tract and to the invariant AG dinucleotide at the 3′ splice site (Voith von Voithenberg et al., 2016). Furthermore, exons with low GC content generally display a higher density of U2AF65 binding sites and are more dependent on U2 snRNP (Lemaire et al., 2019). Thus, to test whether Sam68 interferes with U2AF recruitment, we first conducted UV light-induced cross-linking immunoprecipitation (CLIP) experiments to monitor Sam68 binding to the 3′ splice site region of upregulated exons at P10. Sam68 efficiently bound in proximity of the 3′ splice site of the Arhgef9- and *Arhgap12*-regulated exons with respect to non-regulated exons (Figures 5D and 5E). More importantly, CLIP experiments indicated that U2AF65 was recruited more efficiently to the 3′ splice site of regulated exons in *Sam68*^{KO} cerebella (Figures 5F, 5G, S6F, and S6G). In contrast, no significant change was observed in non-regulated exons of the same pre-mRNAs or in U2AF65 expression levels (Figure 5H). Furthermore, *in vitro* RNA pull-down assays showed that overexpression of Myc-Sam68 also inhibits U2AF65 binding to the *Arhgef9* and *Arhgap12* 3′ splice site probes in the absence of concurrent splicing (Figures S6H and S6I). These results indicate that Sam68 specifically competes with U2AF for recognition of exons characterized by a weak branchpoint.

Sam68 Ablation Alters Post-natal Cerebellar Development

Synaptogenesis and synaptic functions are prominent biological processes associated with Sam68-regulated genes in the cerebellum (Figures S4C and S4D). Moreover, several Sam68 targets are involved in brain development (i.e., *Sema6*, *Epha6*, and *Arhgap12*; Ba et al., 2016; Das et al., 2016; Kerjan et al., 2005) or in neurodevelopmental disorders like ASD (i.e., *Syngap1*, *Mbd5*, and *Arhgef9*; Klein et al., 2017; Satterstrom et al., 2020). Morphological examination of *Sam68*^{KO} cerebellum at P10 revealed an altered foliation pattern with lack of the intercrural fissure between lobules VI and VII (Figure 6A), a defect that was maintained until adulthood (Figure S7A). Staining of PCs with Calbindin 1 (CALB+) showed reduced expansion of the ML in lobules VII and VIII (Figures 6B and 6C) posterior to the intercrural fissure. In contrast, no differences were observed in more anterior (III, IV–V, and VI) and posterior lobules (IX) (Figures 6C and S7B). Furthermore, *Sam68*^{KO} cerebella displayed more proliferating GCs specifically in lobules VII and VIII (Figure S7C), which was paralleled by an increase in EGL thickness (Figure 6C). Thus, lack of Sam68 alters the developmental program of the cerebellum, particularly in the late-differentiating central zone (Legué et al., 2016).

PCs are still immature at P10, with dendrites organized in random orientation within the distal part of the ML (Figures 6B and 6D). In line with a maturation defect, PC arborization was

Figure 4. Sam68 Orchestrates a Developmentally Regulated Splicing Program in the Cerebellum

(A and B) Left: pie charts of the percentage of regulated AS events in *Sam68*^{KO} versus wild-type (WT) cerebellum at P1 (A) and P10 (B). Right: pie charts showing the percentage of up- and downregulated events.

(C) Overlap between AS- and IR-regulated events during development (blue) and events regulated at P1 (orange) or P10 (green) in *Sam68*^{KO} mice.

(D) Enrichment analysis of developmentally regulated events sensitive to Sam68 ablation at P1 and P10 (population n = 10,890).

(E) Overlap between ASD-linked genes (population n = 669) and Sam68-regulated genes (n = 66 of 535).

(F) Left panel: RT-PCR analyses of AS events differentially regulated in WT and *Sam68*^{KO} cerebella at different ages. Right panel: PSI levels from RT-PCR analysis. Mean ± SEM, n = 4; two-way ANOVA, Sidak's multiple comparisons test. WT and *Sam68*^{KO} different ages related to E15.5: *p < 0.05, **p < 0.01, ***p < 0.001, ****p < 0.0001. WT versus *Sam68*^{KO} at each age: §p < 0.05, §§p < 0.01, §§§p < 0.001, §§§§p < 0.0001.

See also Figure S4 and Table S4.

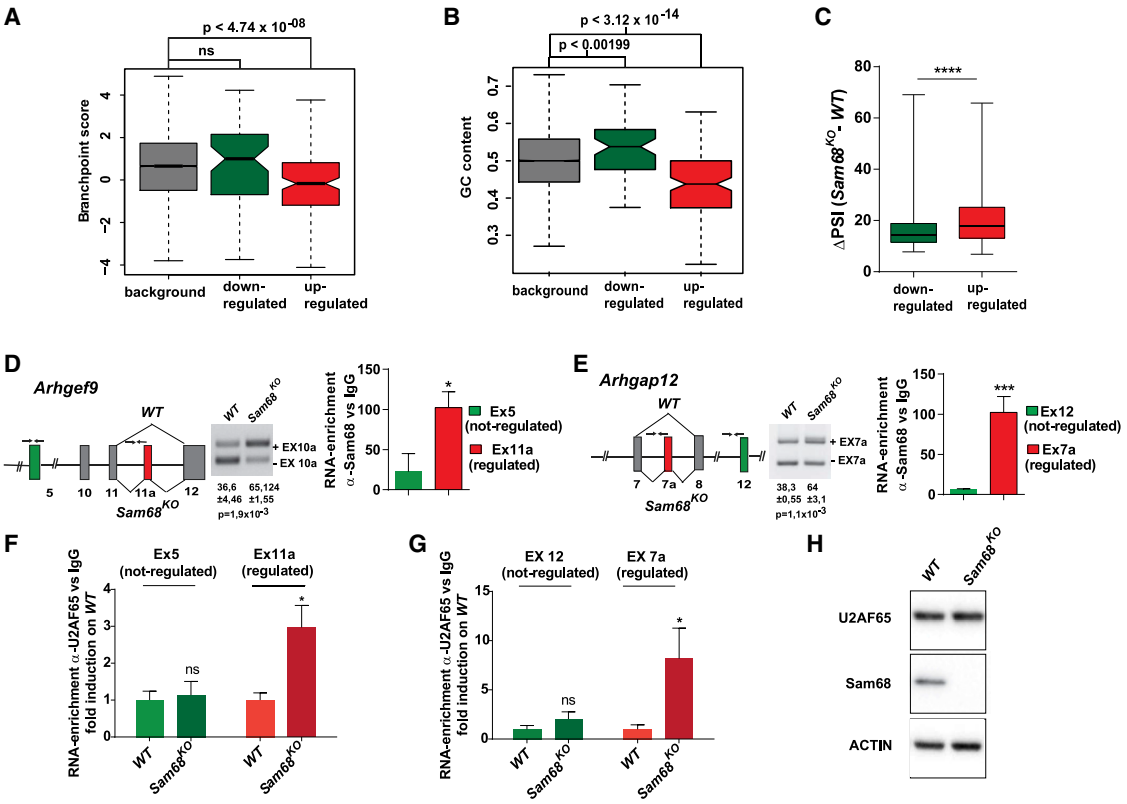

Figure 5. Sam68 Preferentially Represses Exons Characterized by a Weak Branchpoint

5368289352488500(A and B) Branchpoint score (A) and GC content (B) for up- and downregulated exons in *Sam68*^{KO} cerebella with respect to non-regulated exons (Wilcoxon rank-sum test).

(C) Distribution of the ΔPSI of exons differentially regulated between *Sam68*^{KO} and WT cerebella. Whiskers indicate 1.5 interquartile range. Welch's t test; ****p < 0.0001.

(D and E) Left panels: scheme of the AS region of the *Arhgef9* (D) and *Arhgap12* (E) gene, with regulated (red) and constitutive exons (green) and qPCR primers (arrows) and the splicing events in WT and *Sam68*^{KO} cerebella. Shown is RT-PCR analysis for *Sam68*-regulated events in *Arhgef9* (D) and *Arhgap12* (E) with PSI values from densitometric analysis (mean ± SEM, n = 6, paired t test). Right panels: bar graphs showing qPCR analyses of Sam68 CLIPs for *Arhgef9* (D) and *Arhgap12* (E) pre-mRNAs in P10 mouse cerebella. Immunoglobulin G (IgG) was used as a control (mean ± SEM, n = 5, two tailed paired t test, *p < 0.05).

(F and G) qPCR analyses of U2AF65 CLIPs for *Arhgef9* (F) and *Arhgap12* (G) pre-mRNAs in WT and *Sam68*^{KO} P10 cerebella (mean ± SEM, n = 5, multiple Student's t test, *p < 0.05).

(H) Western blot analysis of U2AF65 and Sam68 expression in WT and *Sam68*^{KO} P10 mouse cerebella.

See also Figure S5.

reduced in *Sam68*^{KO} cerebella (Figure 6D). PC maturation is favored by establishment of functional synaptic contacts with afferent fibers, a process correlating with a switch from presynaptic vesicular glutamate transporter 2 (VGLUT2) with vesicular glutamate transporter 1 (VGLUT1) (Miyazaki et al., 2003). Analysis of co-localization between VGLUT1, as marker of mature GC parallel fibers, and CALB signals documented a dramatic reduction in the number of synaptic connections in the central lobules of the *Sam68*^{KO} cerebellum (Figures 6E and 6F), indicating a defect in formation of mature synapses between PCs and GCs. Accordingly, although, in WT mice, the VGLUT2-to-VGLUT1 switch had already occurred at P10, and VGLUT2 prevalently marked distal portions of the PC dendritic tree, its expression was more widely distributed in the whole ML region of the *Sam68*^{KO} cortex (Figure S7D). These results highlight impairment of proper synaptic connections between GCs and PCs in *Sam68*^{KO} cerebella.

Sam68^{KO} Mice Display Impaired Glutamatergic Synaptic Responses and Defects in Motor Coordination and Social Behavior

Refinement of glutamatergic synapses formed by parallel and climbing fibers is required for maturation of cerebellar circuits (Hashimoto and Kano, 2003). To test whether altered maturation of synapses during *Sam68*^{KO} cerebellar development resulted in permanent functional impairment, we performed whole-cell voltage-clamp recordings in PCs of adult mice as a readout of GC pre-synaptic activity. The frequency of spontaneous excitatory post-synaptic currents (sEPSCs) was strikingly reduced (>2.6-fold) in *Sam68*^{KO} PCs (Figures 7A and 7B). Reduced frequency was also observed when miniature excitatory post-synaptic currents (mEPSCs) were recorded after blocking presynaptic action potentials by tetrodotoxin (TTX) (Figure 7C), suggesting that it results from a combination of low presynaptic release probability and reduced number of functional synaptic

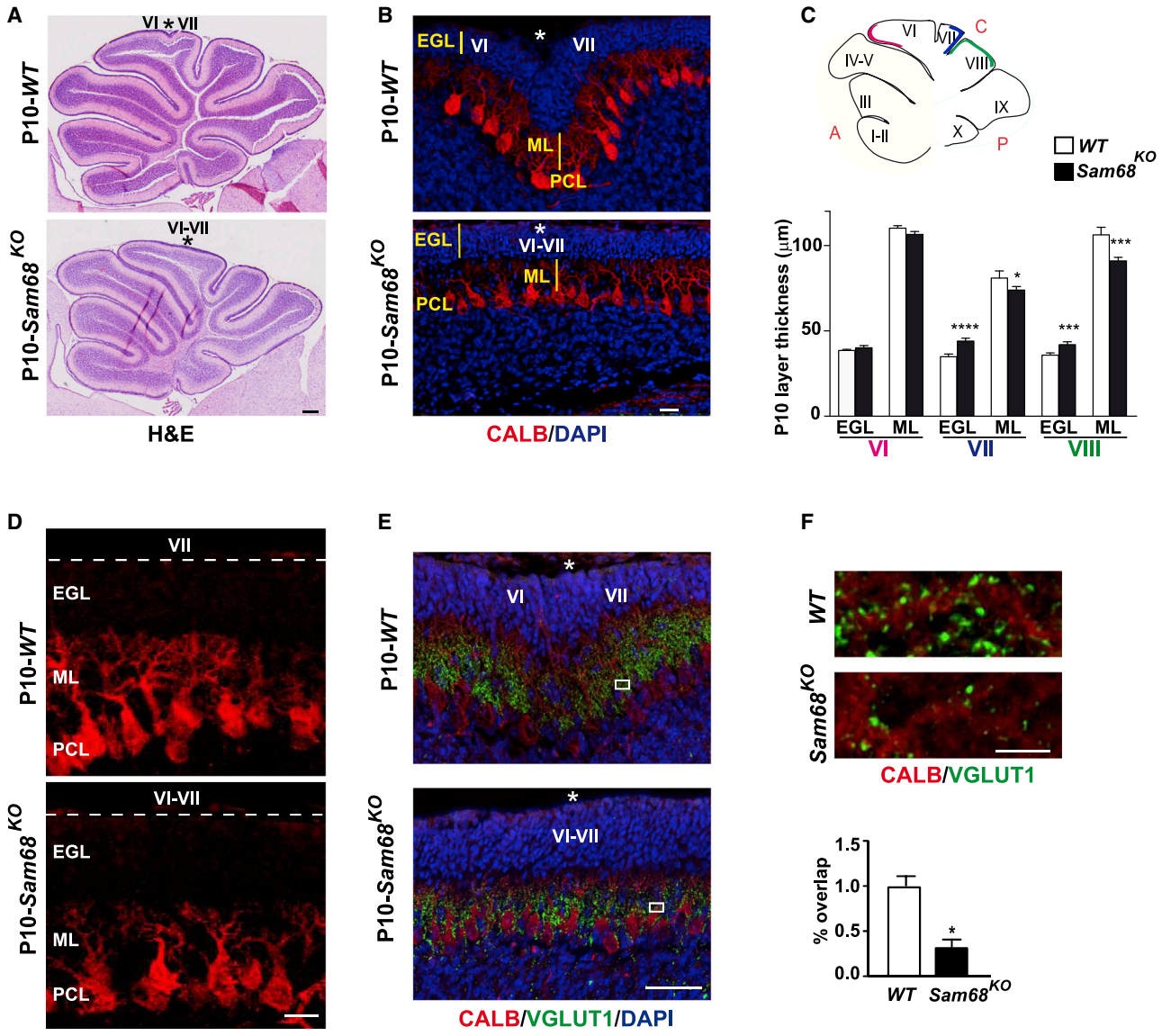

Figure 6. *Sam68*^{KO} Mice Display Defects in Cerebellar Foliation, PC Maturation, and Glutamatergic Synapses

(A) Hematoxylin and eosin (H&E)-stained sections of P10 cerebella from WT and *Sam68*^{KO} mice. The intercrural fissure location is indicated (*). Scale bar, 200 μm.

(B) DAPI nuclear staining and CALB immunofluorescence labeling of PCs in a P10 cerebellar cortex. Images show reduced thickness of the ML (yellow bar) in a *Sam68*^{KO} cortex. Scale bar, 20 μm.

(C) Quantification of average thickness of the EGL and ML in central lobes (c) of WT and *Sam68*^{KO} mice at P10 (mean ± SEM, n = 3/group; unpaired t test, *p < 0.05, **p < 0.01, ***p < 0.001, ****p < 0.0001). Red, blue, and green in the scheme above the graph indicate the regions analyzed in the vermis. A, anterior; C, central; p, posterior.

(D and E) P10 cerebellar sagittal sections immunostained for CALB (D; scale bar, 20 μm) or CALB and VGLUT1 (E; scale bar, 50 μm). White boxes indicate representative regions shown at higher magnification in the top panels in (F) (scale bar, 5 μm).

(F) Bottom panel: quantitative co-localization analysis of mean overlap coefficients of VGLUT1/CALB (unpaired t test, *p < 0.05).

See also Figure S6.

connections. Furthermore, we registered a significant reduction in current amplitude (Figure 7B), highlighting defects in the post-synaptic compartment. Thus, Sam68 function is required for proper cortical connectivity.

Cerebellar defects can be associated with a deficit of motor function and ataxia. Notably, genes regulated by Sam68 are significantly associated with spinocerebellar ataxia (Figure S4E). For instance, *Atxn2* is linked to spinocerebellar ataxia type 2 (SCA2), a syndrome characterized by slow firing frequency of PCs (Dell'Orco et al., 2017), as observed in *Sam68*^{KO} mice. Accordingly, locomotion defects in *Sam68*^{KO} mice have been reported (Lukong and Richard, 2008; Iijima et al., 2011). In line with these observations, *Sam68*^{KO} mice displayed an ataxic phenotype and retracted their hindlimbs in a clasping reflex when

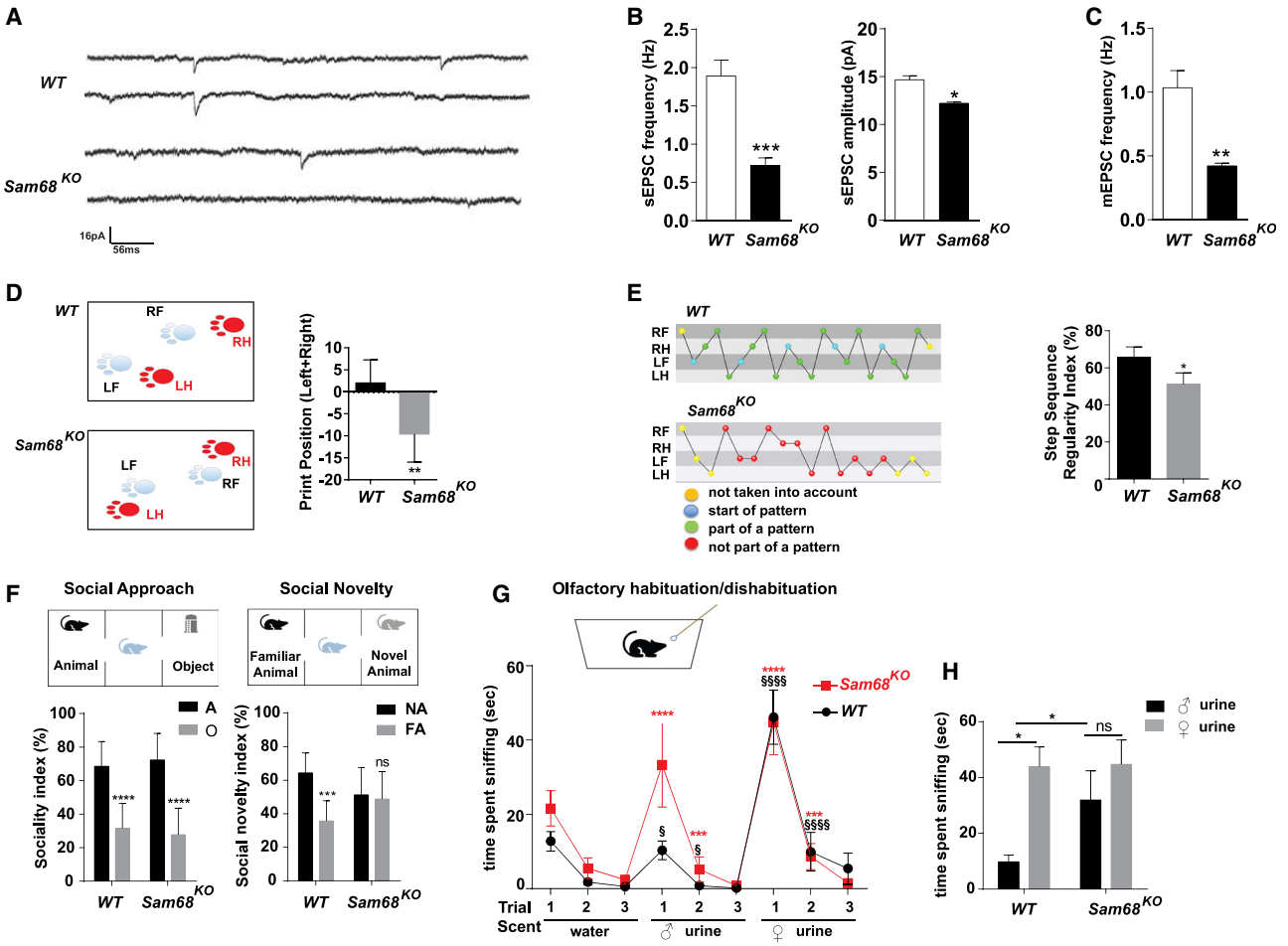

Figure 7. *Sam68*^{KO} Mice Exhibit Defective Motor and Social Behavior

(A) Traces of whole-cell patch-clamp recordings of sEPSCs from adult WT and *Sam68*^{KO} PCs.

(B) Bar graphs showing the average sEPSC frequency (left) and amplitude (right) in WT (n = 17) and *Sam68*^{KO} (n = 24) PCs.

(C) Frequency of miniature EPSCs in whole-cell patch-clamp recordings in WT (n = 7) and *Sam68*^{KO} (n = 7) PCs treated with TTX.

(B and C) Mean ± SEM. One-way ANOVA post hoc comparisons, WT versus *Sam68*^{KO}: *p < 0.05, **p < 0.01, ***p < 0.001.

(D and E) CatWalk gait analysis of print position (D) and step sequence regularity index (E) of P45 male WT (n = 10) and *Sam68*^{KO} (n = 11) mice.

(D) The scheme shows the position of the hindpaw (red print) with respect to the forepaw of the previous step (blue print). Bar graph: + indicates that the hindpaw was placed behind the position of the forepaw of the previous step, 0 at the previous forepaw position, and – in front of the previous forepaw position.

(E) Footfall pattern diagram in WT and *Sam68*^{KO}mice. The regularity index reports the number of normal step sequence patterns relative to the total number of paw placements. RF, right forepaw; RH, right hindpaw; LF, left forepaw; LH, left hindpaw (unpaired t test with Welch's correction; *p < 0.05, **p < 0.01, ***p < 0.001, ****p < 0.0001). In all plots, mean with 95% confidence interval (CI) is shown.

(F) Three-chambered test. Top panel: scheme of the apparatus. Bottom panel: social approach (left panel) evaluates preference for an animal (A) over an object (O), measured by the percentage of time spent in close interaction with A or O/time with A+O (sociality index). The social novelty preference test (right panel) evaluates time spent in close interaction with a familiar animal (FA) or novel animal (NA)/time with FA+NA (social novelty index). Data are expressed as mean ± SEM. WT n = 11, *Sam68*^{KO} n = 11; two-way ANOVA, Sidak's multiple comparisons test; ***p < 0.001; ****p < 0.0001.

(G) Habituation/dishabituation test of WT and *Sam68*^{KO} mice. Data are expressed as mean ± SEM (n = 11) and analyzed by repeated-measures ANOVA followed by Fisher's PLSD post hoc test for comparison of swab presentation by odor for each genotype (for the WT: §p < 0.05, §§§§p < 0.0001; for *Sam68*^{KO}: ****p < 0.0001, ***p < 0.001.

(H) Bar graph indicating the time spent sniffing the two social odors (male, black bar; female, gray bar). Two-way ANOVA, Sidak's multiple comparisons test (mean ± SEM, n = 11; *p < 0.05).

See also Figure S7.

picked up by the tail (Figure S8A). To gain further insights into their motor deficits, we monitored mouse movements with the CatWalk gait system. Paw print area analysis, which indicates the average area of each paw print over a 4-step cycle sequence, and stand index analysis, which measures the ratio of all maximum paw stance values over stance duration, demonstrated specific defects in spatial parameters of the hindlimbs of *Sam68*^{KO} mice (Figures S8B and S8C). Analysis of motor coordination parameters, such as print position and step sequence regularity, showed clear defects in *Sam68*^{KO} mice, which placed

their hindpaws in front of the preceding forepaws, unlike WT mice (Figure 7D). *Sam68*^{KO} mice also displayed lower step regularity (Figure 7E), which resembled ataxic gait phenotypes of other mouse models of cerebellar ataxia and PC disfunction (Lucas et al., 2015).

Aberrant cerebellar development is associated with ASD (Wang et al., 2014), and splicing of many ASD-related genes is altered in *Sam68*^{KO} mice. Moreover, alterations in lobules VI and VII has also been observed in ASD patients (Courchesne et al., 1994; Scott et al., 2009). Thus, we tested whether Sam68 expression affects social behaviors. In the three-chamber test, *Sam68*^{KO} mice displayed a normal social approach and preferred interaction with the animal with respect to the object (Figure 7F). However, when exposed to social novelty, *Sam68*^{KO} mice did not preferentially interact with the novel mouse with respect to the familiar one (Figure 7F). Motor defects did not contribute to social impairment; exploratory ability and chamber preference during habituation were unaffected (Figures S8D and S8E).

In rodents, social interactions strongly depend on olfactory cues (Arakawa et al., 2008), and altered responses to social odors have also been reported in ASD patients (Endevelt-Shapira et al., 2018). *Sam68*^{KO} mice did not show overt olfactory defects and found food without latency (Figure S8F), but they displayed abnormal discrimination of social smells. The olfactory habituation/dishabituation task assay indicated that WT and knockout mice recognized a new smell and rapidly adapted to it (Figure 7G). However, *Sam68*^{KO} mice were unable to discriminate between male and female urine, indicating a specific impairment of social olfactory behavior (Figure 7H).

DISCUSSION

Postnatal cerebellar development is a sensitive period for acquisition of motor and cognitive functions. Disruption of gene expression programs and/or injury of the cerebellum at birth result in high risk of onset of neurodevelopmental disorders (Sathyanesan et al., 2019; Wang et al., 2014). Here we uncovered a highly dynamic splicing program that is set in motion during post-natal development of the cerebellum, involving timely modulation of hundreds of splicing events. Such widespread reprogramming of the cerebellar transcriptome by splicing regulation parallels what has been observed during cortical development (Weyn-Vanhentenryck et al., 2018), indicating that splicing changes are crucial for brain development. Many splicing-modulated genes (~12%) are associated with ASD, suggesting that disruption of the cerebellar splicing program in early life may contribute to cognitive dysfunction. Moreover, Sam68 is required for a significant fraction of these AS events, and its knockout resulted in delayed differentiation of cerebellar structures and permanent impairment of glutamatergic synaptic transmission. *Sam68*^{KO} mice also display defects in motor and social behavior. Thus, our findings suggest that splicing modulation is a key regulatory layer of the gene expression program required for proper cerebellar development and function.

It has been proposed previously that isoform diversity in the developing cerebellum is mainly achieved through alternative promoter and alternative termination regulation (Pal et al., 2011). However, we found that modulation of alternative exons and introns within the coding unit of genes substantially contributes to the complexity of the cerebellar transcriptome. Moreover, despite the diverse nature of the datasets, we observed a large overlap of splicing regulation between the two studies. The fewer AS events found in the previous dataset may be due to the small length and depth of reads used to generate it, which may have limited detection of exon-exon junctions. Our work also reveals a remarkably high level of AS conservation in mouse and human cerebellum development, supporting the physiological relevance of this process across evolution.

Splicing-regulated genes are enriched in functional categories related to cytoskeleton and synapse organization, suggesting that specific splice variants may serve to fine-tune essential developmental processes, such as establishment of synaptic connections and migration of neurons in the cerebellar cortex (Sillitoe and Joyner, 2007). In support of this hypothesis, several genes related to cytoskeleton organization are differentially spliced in the EGL and IGL regions at a time when GCs massively migrate within the cerebellar cortex (Legué et al., 2016). Likewise, AS of several synaptic genes was modulated by GC activation. Thus, the timing of these splicing events correlates with specific processes occurring in cerebellar neurons, suggesting their direct functional effect on the developmental program of the cerebellum.

Our analysis identified six temporal clusters of AS events characterized by enrichment in binding sites for specific splicing factors, including some known to play a role in the cerebellum. For instance, cluster 1 exons, which are progressively included upon development, are enriched for RBFOX2/3 binding sites in the downstream intron, a feature associated with RBFOX-mediated inclusion (Weyn-Vanhentenryck et al., 2014). Notably, RBFOX2 expression is required for proper cerebellum development (Gehman et al., 2012). We opted to focus on Sam68 because its sequence motif was enriched in the majority of the developmental clusters. Indeed, knockout of Sam68 expression affected a wide range of AS events, supporting its key contribution to execution of the splicing program that shapes the cerebellar transcriptome during development. We noted that, although Sam68 expression was not developmentally regulated, its effect on splicing of some exons was age dependent. Because Sam68 splicing activity can be modulated by neuronal activation (Iijima et al., 2011), it is possible that activation of cerebellar circuits may differentially affect some target exons. Alternatively, Sam68 may require co-factors that change in expression during cerebellar development, as observed in the developing cortex, where several splicing factors are expressed in a timely manner and cooperate in splicing decisions (Weyn-Vanhentenryck et al., 2018).

Sam68 mainly represses exons characterized by weak branchpoint sequences and low GC content in the cerebellum. Its effect on splicing appears to require direct binding near the 3′ splice site and competition with the U2AF complex. Notably, a recent report documented that exons characterized by low GC content usually display higher heterogeneity in branchpoint sequence and higher density of U2AF65 binding sites, generally relying more on U2 snRNP binding (Lemaire et al., 2019). In contrast, exons downregulated in *Sam68*^{KO} mice were

characterized by higher GC content, a feature shown to stabilize U1 snRNP binding at the 5′ splice site (Lemaire et al., 2019). Thus, Sam68 may positively regulate their splicing by favoring U1 snRNP recruitment, as we have shown recently in another context (Naro et al., 2019).

Sam68 target genes are enriched in functional categories related to synaptic function and ASD, a syndrome characterized by structural and functional synaptic abnormalities (Sathyanesan et al., 2019). Accordingly, we found several synaptic defects in *Sam68*^{KO} mice. Such defects may be due to the aberrant function of the isoforms produced, like in the case of the *Gria2* ORF disruption that leads to lower expression of this glutamate receptor subunit, possibly causing the reduced amplitude of currents observed in *Sam68*^{KO} PCs. Furthermore, the Sam68-regulated exon in *Nrxn1* confers selectivity for post-synaptic glutamatergic receptors (Dai et al., 2019). Likewise, inclusion of Sam68-regulated exon 11a (62 base pairs) in *Arghef9* introduces a stop codon and yields a shorter protein isoform with a different carboxyl terminus (Harvey et al., 2004), which may assemble with a different network of proteins in the post-synaptic compartment. Thus, dysregulation of the timely expression of multiple synaptic splice variants may underlie the defects in specification of synapses on the somata and dendrites of PC cells observed in the *Sam68*^{KO} cerebellum. Importantly, such defects ultimately result in permanent impairment of glutamatergic transmission in adult mice. A role of Sam68 in establishing functional synapses through translational regulation of target mRNAs has been reported previously in the hippocampus (Klein et al., 2013; Klein et al., 2019). However, because Sam68 is almost exclusively localized in the nucleus in GCs and PCs (Iijima et al., 2011), its role in splicing is likely more relevant in the cerebellum.

Post-natal development is a sensitive period for the cerebellum (Wang et al., 2014) and dysregulation of the splicing program at this stage may contribute to long-lasting motor and cognitive effects. In line with this hypothesis, adult *Sam68*^{KO} mice displayed defects related to gait coordination as well as social deficits associated with ASD, like the inability to discriminate social novelty and social smell cues. Importantly, ASD children have also been shown to exhibit gait and motor coordination defects (Rinehart et al., 2006), and an altered response to social smells was observed in adult ASD patients (Endevelt-Shapira et al., 2018). Thus, although we cannot rule out that defects in other brain regions of *Sam68*^{KO} mice also contribute to these phenotypes, our findings suggest a causal link between splicing dysregulation of ASD-associated genes in the developing cerebellum and onset of ataxia and abnormal social behaviors.

The fissure separating lobules VI and VII in the central zone of the cerebellum is particularly sensitive to Sam68 dosage, likely because of delayed migration of GCs in this region. Lobules VI and VII are engaged in cognitive functions related to social behavior through connectivity with cortical areas in the forebrain (Badura et al., 2018; Wang et al., 2014), and these circuits are altered in ASD patients (Stoodley et al., 2017). It is also interesting to note that, although other STAR family members are conserved in yeast (i.e., SF1) or invertebrates (GLD-1 and QKI in *C. elegans* and *H. sapiens*, respectively), the Sam68 subfamily is only present in higher vertebrates (Ehrmann et al., 2013). These observations suggest that acquisition of Sam68 function correlated with more evolved cognitive functions of the cerebellum in higher vertebrates and that Sam68 inactivation may dysregulate splicing of ASD-linked genes, representing a risk factor for cerebellum-associated neurodevelopmental disorders.

STAR★METHODS

Detailed methods are provided in the online version of this paper and include the following:

- KEY RESOURCES TABLE
- RESOURCE AVAILABILITY
  - Lead Contact
  - Materials Availability
  - Data and Code Availability
- EXPERIMENTAL MODEL AND SUBJECT DETAILS
  - Mouse Husbandry
  - Primary Cerebellar Granule Cell Culture
- METHOD DETAILS
  - RNA Isolation and RT-PCR
  - RNA-sequencing Analysis
  - Functional Enrichment Analysis
  - Laser-Capture Microdissection
  - Binding Motif Enrichment Analysis
  - Protein Extracts and Western Blot analysis
  - Crosslinking-Immunoprecipitation Experiment
  - RNA pull-down
  - Histology, immunohistochemistry and colocalization analysis
  - BrdU incorporation
  - Antibodies Used for Immunofluorescence Labeling
  - Electrophysiology
  - CatWalk Test
  - Social approach and social novelty preference assay
  - Olfactory tests
- QUANTIFICATION AND STATISTICAL ANALYSIS

SUPPLEMENTAL INFORMATION

Supplemental Information can be found online at https://doi.org/10.1016/j.celrep.2020.107703.

ACKNOWLEDGMENTS

We thank Drs A. Primerano, D. Fresegna, C. Catale, and S. Bussone for technical assistance; M.C. Geloso, P. Bielli, and M.T. Viscomi for critical discussions; and T. Durbic (Donnelly Sequencing Centre) for generating RNA sequencing data. C.N. was supported by a fellowship from Fondazione Umberto Veronesi. This work was supported by grants from the Associazione Italiana Ricerca sul Cancro (IG23416) and the Italian Ministry of University and Research (PRIN 2017) (to C.S.) and a foundation grant from the Canadian Institutes of Health Research (to B.J.B.). Università Cattolica del Sacro Cuore contributed to the funding of this research project and its publication.

AUTHOR CONTRIBUTIONS

Conceptualization, D.F., D.C., D.M., V.C., A.M., and C.S.; Methodology, D.F., A.M., and D.M.; Software, Formal Analysis, and Data Curation, R.J.W. and A.M.; Investigation, D.F., E.C., G.L.S., C.N., V.P., D.B., V.M., M.G., C.D.P., and F.R.R.; Writing, D.F., R.J.W., B.J.B., and C.S.; Supervision, D.C., D.M., and C.S.; Project Administration and Funding Acquisition, B.J.B. and C.S.

DECLARATION OF INTERESTS

The authors declare no competing interests.

Received: October 14, 2019
Revised: March 13, 2020
Accepted: May 7, 2020
Published: June 2, 2020

REFERENCES

Arakawa, H., Blanchard, D.C., Arakawa, K., Dunlap, C., and Blanchard, R.J. (2008). Scent marking behavior as an odorant communication in mice. Neurosci. Biobehav. Rev. *32*, 1236–1248.

Ba, W., Selten, M.M., van der Raadt, J., van Veen, H., Li, L.L., Benevento, M., Oudakker, A.R., Lasabuda, R.S.E., Letteboer, S.J., Roepman, R., et al. (2016). ARHGAP12 Functions as a Developmental Brake on Excitatory Synapse Function. Cell Rep. *14*, 1355–1368.

Badura, A., Verpeut, J.L., Metzger, J.W., Pereira, T.D., Pisano, T.J., Deverett, B., Bakshinskaya, D.E., and Wang, S.S. (2018). Normal cognitive and social development require posterior cerebellar activity. eLife *7*, e36401.

Basu, S.N., Kollu, R., and Banerjee-Basu, S. (2009). AutDB: a gene reference resource for autism research. Nucleic Acids Res. *37*, D832–D836.

Bielli, P., and Sette, C. (2017). Analysis of in vivo Interaction between RNA Binding Proteins and Their RNA Targets by UV Cross-linking and Immunoprecipitation (CLIP) Method. Bio. Protoc. *7*, e2274.

Bolger, A.M., Lohse, M., and Usadel, B. (2014). Trimmomatic: a flexible trimmer for Illumina sequence data. Bioinformatics *30*, 2114–2120.

Chang, S.H., Gao, L., Li, Z., Zhang, W.N., Du, Y., and Wang, J. (2013). BDgene: a genetic database for bipolar disorder and its overlap with schizophrenia and major depressive disorder. Biol. Psychiatry *74*, 727–733.

Corvelo, A., Hallegger, M., Smith, C.W., and Eyras, E. (2010). Genome-wide association between branch point properties and alternative splicing. PLoS Comput. Biol. *6*, e1001016.

Courchesne, E., Saitoh, O., Yeung-Courchesne, R., Press, G.A., Lincoln, A.J., Haas, R.H., and Schreibman, L. (1994). Abnormality of cerebellar vermian lobules VI and VII in patients with infantile autism: identification of hypoplastic and hyperplastic subgroups with MR imaging. AJR Am. J. Roentgenol. *162*, 123–130.

Dai, J., Aoto, J., and Sudhof, T.C. (2019). Alternative Splicing of Presynaptic Neurexins Differentially Controls Postsynaptic NMDA and AMPA Receptor Responses. Neuron *102*, 993–1008.e5.

Danilenko, M., Dalgliesh, C., Pagliarini, V., Naro, C., Ehrmann, I., Feracci, M., Kheirollahi-Chadegani, M., Tyson-Capper, A., Clowry, G.J., Fort, P., et al. (2017). Binding site density enables paralog-specific activity of SLM2 and Sam68 proteins in Neurexin2 AS4 splicing control. Nucleic Acids Res. *45*, 4120–4130.

Das, G., Yu, Q., Hui, R., Reuhl, K., Gale, N.W., and Zhou, R. (2016). EphA5 and EphA6: regulation of neuronal and spine morphology. Cell Biosci. *6*, 48.

Dell'Orco, J.M., Pulst, S.M., and Shakkottai, V.G. (2017). Potassium channel dysfunction underlies Purkinje neuron spiking abnormalities in spinocerebellar ataxia type 2. Hum. Mol. Genet. *26*, 3935–3945.

Ehrmann, I., Dalgliesh, C., Liu, Y., Danilenko, M., Crosier, M., Overman, L., Arthur, H.M., Lindsay, S., Clowry, G.J., Venables, J.P., et al. (2013). The tissue-specific RNA binding protein T-STAR controls regional splicing patterns of neurexin pre-mRNAs in the brain. PLoS Genet. *9*, e1003474.

Ehrmann, I., Gazzara, M.R., Pagliarini, V., Dalgliesh, C., Kheirollahi-Chadegani, M., Xu, Y., Cesari, E., Danilenko, M., Maclennan, M., Lowdon, K., et al. (2016). A SLM2 Feedback Pathway Controls Cortical Network Activity and Mouse Behavior. Cell Rep. *17*, 3269–3280.

Endevelt-Shapira, Y., Perl, O., Ravia, A., Amir, D., Eisen, A., Bezalel, V., Rozenkrantz, L., Mishor, E., Pinchover, L., Soroka, T., et al. (2018). Altered responses to social chemosignals in autism spectrum disorder. Nat. Neurosci. *21*, 111–119.

Feracci, M., Foot, J.N., Grellscheid, S.N., Danilenko, M., Stehle, R., Gonchar, O., Kang, H.S., Dalgliesh, C., Meyer, N.H., Liu, Y., et al. (2016). Structural basis of RNA recognition and dimerization by the STAR proteins T-STAR and Sam68. Nat. Commun. *7*, 10355.

Fu, X.D., and Ares, M., Jr. (2014). Context-dependent control of alternative splicing by RNA-binding proteins. Nat. Rev. Genet. *15*, 689–701.

Gehman, L.T., Meera, P., Stoilov, P., Shiue, L., O'Brien, J.E., Meisler, M.H., Ares, M., Jr., Otis, T.S., and Black, D.L. (2012). The splicing regulator Rbfox2 is required for both cerebellar development and mature motor function. Genes Dev. *26*, 445–460.

Harvey, K., Duguid, I.C., Alldred, M.J., Beatty, S.E., Ward, H., Keep, N.H., Lingenfelter, S.E., Pearce, B.R., Lundgren, J., Owen, M.J., et al. (2004). The GDP-GTP exchange factor collybistin: an essential determinant of neuronal gephyrin clustering. J. Neurosci. *24*, 5816–5826.

Hashimoto, K., and Kano, M. (2003). Functional differentiation of multiple climbing fiber inputs during synapse elimination in the developing cerebellum. Neuron *38*, 785–796.

Heck, J., Parutto, P., Ciuraszkiewicz, A., Bikbaev, A., Freund, R., Mitlohner, J., Alonso, M., Fejtova, A., Holcman, D., and Heine, M. (2019). Transient Confinement of CaV2.1 Ca(2+)-Channel Splice Variants Shapes Synaptic Short-Term Plasticity. Neuron *103*, 66–79.e12.

Iijima, T., Wu, K., Witte, H., Hanno-Iijima, Y., Glatter, T., Richard, S., and Scheiffele, P. (2011). SAM68 regulates neuronal activity-dependent alternative splicing of neurexin-1. Cell *147*, 1601–1614.

Irimia, M., Weatheritt, R.J., Ellis, J.D., Parikshak, N.N., Gonatopoulos-Pournatzis, T., Babor, M., Quesnel-Vallières, M., Tapial, J., Raj, B., O'Hanlon, D., et al. (2014). A highly conserved program of neuronal microexons is misregulated in autistic brains. Cell *159*, 1511–1523.

Jeyabalan, N., and Clement, J.P. (2016). SYNGAP1: Mind the Gap. Front. Cell. Neurosci. *10*, 32.

Kerjan, G., Dolan, J., Haumaitre, C., Schneider-Maunoury, S., Fujisawa, H., Mitchell, K.J., and Chédotal, A. (2005). The transmembrane semaphorin Sema6A controls cerebellar granule cell migration. Nat. Neurosci. *8*, 1516–1524.

Klein, M.E., Younts, T.J., Castillo, P.E., and Jordan, B.A. (2013). RNA-binding protein Sam68 controls synapse number and local β-actin mRNA metabolism in dendrites. Proc. Natl. Acad. Sci. USA *110*, 3125–3130.

Klein, K.M., Pendziwiat, M., Eilam, A., Gilad, R., Blatt, I., Rosenow, F., Kanaan, M., Helbig, I., and Afawi, Z.; Israeli-Palestinian Epilepsy Family Consortium (2017). The phenotypic spectrum of ARHGEF9 includes intellectual disability, focal epilepsy and febrile seizures. J. Neurol. *264*, 1421–1425.

Klein, M.E., Younts, T.J., Cobo, C.F., Buxbaum, A.R., Aow, J., Erdjument-Bromage, H., Richard, S., Malinow, R., Neubert, T.A., Singer, R.H., et al. (2019). Sam68 Enables Metabotropic Glutamate Receptor-Dependent LTD in Distal Dendritic Regions of CA1 Hippocampal Neurons. Cell Rep. *29*, 1789–1799.e6.

Kuleshov, M.V., Jones, M.R., Rouillard, A.D., Fernandez, N.F., Duan, Q., Wang, Z., Koplev, S., Jenkins, S.L., Jagodnik, K.M., Lachmann, A., et al. (2016). Enrichr: a comprehensive gene set enrichment analysis web server 2016 update. Nucleic Acids Res. *44* (*W1*), W90-7.

La Rosa, P., Bielli, P., Compagnucci, C., Cesari, E., Volpe, E., Farioli Vecchioli, S., and Sette, C. (2016). Sam68 promotes self-renewal and glycolytic metabolism in mouse neural progenitor cells by modulating *Aldh1a3* pre-mRNA 3′-end processing. eLife *5*, e20750.

Legué, E., Gottshall, J.L., Jaumouillé, E., Roselló-Díez, A., Shi, W., Barraza, L.H., Washington, S., Grant, R.L., and Joyner, A.L. (2016). Differential timing of granule cell production during cerebellum development underlies generation of the foliation pattern. Neural Dev. *11*, 17.

Lemaire, S., Fontrodona, N., Aubé, F., Claude, J.B., Polvèche, H., Modolo, L., Bourgeois, C.F., Mortreux, F., and Auboeuf, D. (2019). Characterizing the interplay between gene nucleotide composition bias and splicing. Genome Biol. *20*, 259.

Levi, G., Aloisi, F., Ciotti, M.T., and Gallo, V. (1984). Autoradiographic localization and depolarization-induced release of acidic amino acids in differentiating cerebellar granule cell cultures. Brain Res. *290*, 77–86.

Love, M.I., Huber, W., and Anders, S. (2014). Moderated estimation of fold change and dispersion for RNA-seq data with DESeq2. Genome Biol. *15*, 550.

Lucas, E.K., Reid, C.S., McMeekin, L.J., Dougherty, S.E., Floyd, C.L., and Cowell, R.M. (2015). Cerebellar transcriptional alterations with Purkinje cell dysfunction and loss in mice lacking PGC-1α. Front. Cell. Neurosci. *8*, 441.

Lukong, K.E., and Richard, S. (2008). Motor coordination defects in mice deficient for the Sam68 RNA-binding protein. Behav. Brain Res. *189*, 357–363.

Maze, I., Wenderski, W., Noh, K.M., Bagot, R.C., Tzavaras, N., Purushothaman, I., Elsässer, S.J., Guo, Y., Ionete, C., Hurd, Y.L., et al. (2015). Critical Role of Histone Turnover in Neuronal Transcription and Plasticity. Neuron *87*, 77–94.

Mazin, P., Xiong, J., Liu, X., Yan, Z., Zhang, X., Li, M., He, L., Somel, M., Yuan, Y., Phoebe Chen, Y.P., et al. (2013). Widespread splicing changes in human brain development and aging. Mol. Syst. Biol. *9*, 633.

Miyazaki, T., Fukaya, M., Shimizu, H., and Watanabe, M. (2003). Subtype switching of vesicular glutamate transporters at parallel fibre-Purkinje cell synapses in developing mouse cerebellum. Eur. J. Neurosci. *17*, 2563–2572.

Moy, S.S., Nadler, J.J., Perez, A., Barbaro, R.P., Johns, J.M., Magnuson, T.R., Piven, J., and Crawley, J.N. (2004). Sociability and preference for social novelty in five inbred strains: an approach to assess autistic-like behavior in mice. Genes Brain Behav. *3*, 287–302.

Naro, C., Pellegrini, L., Jolly, A., Farini, D., Cesari, E., Bielli, P., de la Grange, P., and Sette, C. (2019). Functional Interaction between U1snRNP and Sam68 Insures Proper 3′ End Pre-mRNA Processing during Germ Cell Differentiation. Cell Rep. *26*, 2929–2941.e5.

Pagliarini, V., Pelosi, L., Bustamante, M.B., Nobili, A., Berardinelli, M.G., D'Amelio, M., Musarò, A., and Sette, C. (2015). SAM68 is a physiological regulator of SMN2 splicing in spinal muscular atrophy. J. Cell Biol. *211*, 77–90.

Pal, S., Gupta, R., Kim, H., Wickramasinghe, P., Baubet, V., Showe, L.C., Dahmane, N., and Davuluri, R.V. (2011). Alternative transcription exceeds alternative splicing in generating the transcriptome diversity of cerebellar development. Genome Res. *21*, 1260–1272.

Park, J.W., Jung, S., Rouchka, E.C., Tseng, Y.T., and Xing, Y. (2016). rMAPS: RNA map analysis and plotting server for alternative exon regulation. Nucleic Acids Res. *44* (*W1*), W333-8.

Paronetto, M.P., Achsel, T., Massiello, A., Chalfant, C.E., and Sette, C. (2007). The RNA-binding protein Sam68 modulates the alternative splicing of Bcl-x. J. Cell Biol. *176*, 929–939.

Paronetto, M.P., Messina, V., Barchi, M., Geremia, R., Richard, S., and Sette, C. (2011). Sam68 marks the transcriptionally active stages of spermatogenesis and modulates alternative splicing in male germ cells. Nucleic Acids Res. *39*, 4961–4974.

Quesnel-Vallières, M., Dargaei, Z., Irimia, M., Gonatopoulos-Pournatzis, T., Ip, J.Y., Wu, M., Sterne-Weiler, T., Nakagawa, S., Woodin, M.A., Blencowe, B.J., and Cordes, S.P. (2016). Misregulation of an Activity-Dependent Splicing Network as a Common Mechanism Underlying Autism Spectrum Disorders. Mol. Cell *64*, 1023–1034.

Quesnel-Vallières, M., Weatheritt, R.J., Cordes, S.P., and Blencowe, B.J. (2019). Autism spectrum disorder: insights into convergent mechanisms from transcriptomics. Nat. Rev. Genet. *20*, 51–63.

Raj, B., and Blencowe, B.J. (2015). Alternative Splicing in the Mammalian Nervous System: Recent Insights into Mechanisms and Functional Roles. Neuron *87*, 14–27.

Ray, D., Kazan, H., Cook, K.B., Weirauch, M.T., Najafabadi, H.S., Li, X., Gueroussov, S., Albu, M., Zheng, H., Yang, A., et al. (2013). A compendium of RNA-binding motifs for decoding gene regulation. Nature *499*, 172–177.

Reimand, J., Arak, T., Adler, P., Kolberg, L., Reisberg, S., Peterson, H., and Vilo, J. (2016). g:Profiler-a web server for functional interpretation of gene lists (2016 update). Nucleic Acids Res. *44* (*W1*), W83-9.

Richard, S., Torabi, N., Franco, G.V., Tremblay, G.A., Chen, T., Vogel, G., Morel, M., Cléroux, P., Forget-Richard, A., Komarova, S., et al. (2005). Ablation of the Sam68 RNA binding protein protects mice from age-related bone loss. PLoS Genet. *1*, e74.

Rinehart, N.J., Tonge, B.J., Iansek, R., McGinley, J., Brereton, A.V., Enticott, P.G., and Bradshaw, J.L. (2006). Gait function in newly diagnosed children with autism: Cerebellar and basal ganglia related motor disorder. Dev. Med. Child Neurol. *48*, 819–824.

Rodriques, S.G., Stickels, R.R., Goeva, A., Martin, C.A., Murray, E., Vanderburg, C.R., Welch, J., Chen, L.M., Chen, F., and Macosko, E.Z. (2019). Slide-seq: A scalable technology for measuring genome-wide expression at high spatial resolution. Science *363*, 1463–1467.

Rosenberg, A.B., Roco, C.M., Muscat, R.A., Kuchina, A., Sample, P., Yao, Z., Graybuck, L.T., Peeler, D.J., Mukherjee, S., Chen, W., et al. (2018). Single-cell profiling of the developing mouse brain and spinal cord with split-pool barcoding. Science *360*, 176–182.

Roussignol, G., Ango, F., Romorini, S., Tu, J.C., Sala, C., Worley, P.F., Bockaert, J., and Fagni, L. (2005). Shank expression is sufficient to induce functional dendritic spine synapses in aspiny neurons. J. Neurosci. *25*, 3560–3570.

Sathyanesan, A., Zhou, J., Scafidi, J., Heck, D.H., Sillitoe, R.V., and Gallo, V. (2019). Emerging connections between cerebellar development, behaviour and complex brain disorders. Nat. Rev. Neurosci. *20*, 298–313.

Satterstrom, F.K., Kosmicki, J.A., Wang, J., Breen, M.S., De Rubeis, S., An, J.Y., Peng, M., Collins, R., Grove, J., Klei, L., et al. (2020). Large-Scale Exome Sequencing Study Implicates Both Developmental and Functional Changes in the Neurobiology of Autism. Cell *180*, 568–584.e23.

Scott, J.A., Schumann, C.M., Goodlin-Jones, B.L., and Amaral, D.G. (2009). A comprehensive volumetric analysis of the cerebellum in children and adolescents with autism spectrum disorder. Autism Res. *2*, 246–257.

Sillitoe, R.V., and Joyner, A.L. (2007). Morphology, molecular codes, and circuitry produce the three-dimensional complexity of the cerebellum. Annu. Rev. Cell Dev. Biol. *23*, 549–577.

Stoodley, C.J., D'Mello, A.M., Ellegood, J., Jakkamsetti, V., Liu, P., Nebel, M.B., Gibson, J.M., Kelly, E., Meng, F., Cano, C.A., et al. (2017). Altered cerebellar connectivity in autism and cerebellar-mediated rescue of autism-related behaviors in mice. Nat. Neurosci. *20*, 1744–1751.

Sugawara, T., Hisatsune, C., Miyamoto, H., Ogawa, N., and Mikoshiba, K. (2017). Regulation of spinogenesis in mature Purkinje cells via mGluR/PKC-mediated phosphorylation of CaMKIIβ. Proc. Natl. Acad. Sci. USA *114*, E5256–E5265.

Tapial, J., Ha, K.C.H., Sterne-Weiler, T., Gohr, A., Braunschweig, U., Hermoso-Pulido, A., Quesnel-Vallières, M., Permanyer, J., Sodaei, R., Marquez, Y., et al. (2017). An atlas of alternative splicing profiles and functional associations reveals new regulatory programs and genes that simultaneously express multiple major isoforms. Genome Res. *27*, 1759–1768.

Traunmüller, L., Gomez, A.M., Nguyen, T.M., and Scheiffele, P. (2016). Control of neuronal synapse specification by a highly dedicated alternative splicing program. Science *352*, 982–986.

Vandeputte, C., Taymans, J.M., Casteels, C., Coun, F., Ni, Y., Van Laere, K., and Baekelandt, V. (2010). Automated quantitative gait analysis in animal models of movement disorders. BMC Neurosci. *11*, 92.

Voith von Voithenberg, L., Sánchez-Rico, C., Kang, H.S., Madl, T., Zanier, K., Barth, A., Warner, L.R., Sattler, M., and Lamb, D.C. (2016). Recognition of the 3′ splice site RNA by the U2AF heterodimer involves a dynamic population shift. Proc. Natl. Acad. Sci. USA *113*, E7169–E7175.

Vuong, C.K., Black, D.L., and Zheng, S. (2016). The neurogenetics of alternative splicing. Nat. Rev. Neurosci. *17*, 265–281.

Wang, S.S., Kloth, A.D., and Badura, A. (2014). The cerebellum, sensitive periods, and autism. Neuron *83*, 518–532.

Weatheritt, R.J., Sterne-Weiler, T., and Blencowe, B.J. (2016). The ribosome-engaged landscape of alternative splicing. Nat. Struct. Mol. Biol. *23*, 1117–1123.

Weyn-Vanhentenryck, S.M., Mele, A., Yan, Q., Sun, S., Farny, N., Zhang, Z., Xue, C., Herre, M., Silver, P.A., Zhang, M.Q., et al. (2014). HITS-CLIP and integrative modeling define the Rbfox splicing-regulatory network linked to brain development and autism. Cell Rep. *6*, 1139–1152.

Weyn-Vanhentenryck, S.M., Feng, H., Ustianenko, D., Duffié, R., Yan, Q., Jacko, M., Martinez, J.C., Goodwin, M., Zhang, X., Hengst, U., et al. (2018). Precise temporal regulation of alternative splicing during neural development. Nat. Commun. *9*, 2189.

Wingett, S.W., and Andrews, S. (2018). FastQ Screen: A tool for multi-genome mapping and quality control. F1000Res. *7*, 1338.

Yang, M., and Crawley, J.N. (2009). Simple behavioral assessment of mouse olfaction. Curr. Protoc. Neurosci. *Chapter 8*, Unit 8.24.

Yeo, G., and Burge, C.B. (2004). Maximum entropy modeling of short sequence motifs with applications to RNA splicing signals. J. Comput. Biol. *11*, 377–394.

Zhang, X., Chen, M.H., Wu, X., Kodani, A., Fan, J., Doan, R., Ozawa, M., Ma, J., Yoshida, N., Reiter, J.F., et al. (2016). Cell-Type-Specific Alternative Splicing Governs Cell Fate in the Developing Cerebral Cortex. Cell *166*, 1147–1162.e15.

STAR★METHODS

KEY RESOURCES TABLE

REAGENT or RESOURCE	SOURCE	IDENTIFIER
Antibodies		
Rabbit polyclonal anti-Sam68	Bethyl Laboratories	Cat#A302-110A; RRID:AB_1604289
Donkey whole antibody anti Rabbit IgG HRP-linked	GE Healthcare	Cat# NA934; RRID: AB_772206
Sheep whole antibody anti mouse IgG HRP-linked	GE Healthcare	Cat# NA931; RRID:AB_772210
Alexa Fluor-488 goat anti mouse	Thermo Fisher Scientific	Cat# A11001; RRID:AB_2534069
Alexa Fluor-594 goat anti-rabbit	Thermo Fisher Scientific	Cat# A11037; RRID:AB_2534095
Mouse monoclonal anti 5-bromo-2′-deoxyuridine (BrdU)	Millipore	Cat# 05-633, RRID:AB_11212826
Mouse monoclonal anti CALB1	Sigma-Aldrich	Cat# C9848, RRID:AB_476894
Mouse monoclonal anti-U2AF65	Sigma-Aldrich	Cat#U4758, RRID:AB_262122
Rabbit polyclonal anti VGLUT1	Synaptic System	Cat# 135 303, RRID:AB_887875
Mouse monoclonal anti-ACTIN	Santa Cruz	Cat# sc-47778, RRID: AB_626632
Chemicals, Peptides, and Recombinant Proteins		
Dnase I from bovine pancreas	Sigma Aldrich	Cat# DN25; CAS 9003-98-9
Trypsin from bovine pancreas	Sigma Aldrich	Cat#T8003
Poly-L-lysine	Sigma Aldrich	Cat# P9155
Trypsin inhibitor from bovine pancreas	Sigma Aldrich	Cat#T9003
5-Bromo-2′-deoxyuridine	Sigma Aldrich	Cat#B5002
B27^{tm} Supplement	Thermo Fisher Scientific,GIBCO	Cat#17504-044
(+)-Bicuculline	Tocris	Cat#0130
Tetrodotoxin	Tocris	Cat#1078
RNAprotect Tissue Reagent	QIAGEN	Cat# 76104
Tissue-Tek® O.C.T. Compound	VWR	Cat# 25608-930
RNase away	Sigma Aldrich	Cat# 83931
Proteinase K	Sigma Aldrich	Cat# 03115879001
Protease inhibitor cocktail	Sigma Aldrich	Cat# P8340
DNase RNase-free Turbo	Thermo Fisher Scientific, Ambion	Cat# AM2239
RNasin Ribonuclease Inhibitor	Promega	Cat# N251B
Critical Commercial Assays		
miRNEasy minikit	QIAGEN	Cat# 217004
M-MLV reverse transcriptase	Promega	Cat# M170B
SuperScript^{TM}-IV VILO^{TM} master Mix with EZ DNase^{TM}	Thermo Fisher Scientific, Invitrogen	***Cat# 11766050***
GoTaq	Promega	Cat# M3005
T7 RNA Polymerase	Thermo Fisher Scientific, Ambion	Cat# AM2085
RNasin Ribonuclease Inhibitor	Promega	Cat# N251B
LightCycler 480 SYBR Green I Master	Roche	Cat# 04 887 352 001
Clarity Western ECL Blotting Substrate	Biorad	Cat#1705060
RNase I	Thermo Fisher Scientific, Invitrogen	Cat#AM2295
RNA Labeling Mix	Roche	Cat# 11685597910
Streptavidin-Sepharose high performance	Sigma Aldrich	Cat# GE17-5113-01
Dynabeads Protein G	Thermo Fisher Scientific, Novex	Cat#10004D
4',6-diamidino-2-phenylindole (DAPI)	Thermo Fisher Scientific,	Cat#D1306

(*Continued on next page*)

Continued

REAGENT or RESOURCE	SOURCE	IDENTIFIER
Deposited Data		
Raw and analyzed data	This paper	GEO: GSE133711
Experimental Models: Cell Lines		
Human: HEK293T	Laboratory stock	N/A
Experimental Models: Organisms/Strains		
Mouse: C57BL/6 KHdrbs1tm1Rchd	Richard et al., 2005	N/A
Oligonucleotides		
See Table S5 for primer sequences used for conventional and qRT analysis	This paper	N/A
See Table S5 for primers sequences used for minigenes cloning	This paper	N/A
See Table S5 for primers sequences used for the probe synthesis of RNA pull down experiments	This paper	N/A
Recombinant DNA		
pCDNA3-Myc	Paronetto et al., 2007	N/A
pCDNA3-Myc-Sam68	Paronetto et al., 2007	N/A
pXJ41	Ehrmann et al., 2016	N/A
pXJ41-Arhgap12 ex7a	This paper	N/A
pXJ41-Arhgef9 ex11a	This paper	N/A
Software and Algorithms		
GraphPad Prism 6.0	GraphPad Software	https://www.graphpad.com/
FastqC	Wingett and Andrews, 2018	http://www.bioinformatics.babraham.ac.uk/projects/fastqc/
Imaris		https://imaris.oxinst.com/
ImageJ		https://imagej.nih.gov/
Trimmomatics	Bolger et al., 2014	http://www.usadellab.org/cms/
VAST-TOOLS	Irimia et al., 2014	https://github.com/vastgroup/vast-tools
Deseq2	Love et al., 2014	https://bioconductor.org/packages/release/bioc/html/DESeq2.html
G:Profiler	Reimand et al., 2016	http://biit.cs.ut.ee/gprofiler_archive2/r1760_e93_eg40/web/
ENRICHR	Kuleshov et al., 2016	http://amp.pharm.mssm.edu/Enrichr
SFARI	Basu et al., 2009	https://gene.sfari.org/
BDgene	Chang et al., 2013	http://bdgene.psych.ac.cn
MaxEntScan	Yeo and Burge, 2004	https://omictools.com/maxentscan-tool
rMAPS	Park et al., 2016	http://rmaps.cecsresearch.org/
SVM-BPfinder	Corvelo et al., 2010	https://bitbucket.org/regulatorygenomicsupf/svm-bpfinder
P-CLAMP 10		https://mdc.custhelp.com/
Mini Analysis Version 6.0.7		http://www.synaptosoft.com/
Ethovision XT		https://www.noldus.com/ethovision-xt

RESOURCE AVAILABILITY

Lead Contact

Further information and requests for resources and reagents should be directed to and will be fulfilled by the Lead Contact, Claudio Sette (claudio.sette@unicatt.it).

Materials Availability

Plasmid pXJ41-Arhgap12 ex7a and pXJ41-Arhgef9 ex11a generated in this study are available from the Lead Contact.

Data and Code Availability

The RNaseq data generated in this study are available at NCBI Gene Expression Omnibus (accession number GSE133711).

EXPERIMENTAL MODEL AND SUBJECT DETAILS

Mouse Husbandry

C57BL/6 mice wild-type and *Sam68*^{ko} littermates were maintained on a normal 12 hr light/dark cycle in the animal facility of the Fondazione Santa Lucia IRCCS and genotyped by the Biotool Mouse Direct PCR Kit. Mice breeding, housing, and behavioral tests were conducted according to the Guideline of the Italian Institute of Health (protocol n. 750/2017-PR).

Primary Cerebellar Granule Cell Culture

Cerebellar GC cultures were prepared as indicated in Levi et al. (1984) from both male and female C57BL/6 mouse pups on postnatal days 5. The tissue was dissociated with 0.025% trypsin (Sigma-Aldrich) and neurons were plated into poly-D-lysine-coated dishes (0.5x105/cm2) and maintained for 5 (DIV5) or 10 days (DIV 10) in Neurobasal Medium (Invitrogen) containing 2% B27 supplement, 2 mM glutamine, gentamycin (100 μg/ml) and 50U penicillin/streptomycin (GIBCO). Neurons were fed with a half media exchange every 4 days. For neuronal depolarization experiments, GCs cultures were stimulated with 25 mM KCl (final KCl concentration 30mM) for 3 hr.

METHOD DETAILS

RNA Isolation and RT-PCR

For RNA-seq analysis, cerebella from wild-type and *Sam68*^{ko} male littermates at different ages were isolated and maintained in RNA later stabilization reagent (QIAGEN). Total RNA was extracted and DNase treated using the RNAeasy Mini Kit (QIAGEN) according to manufacturer's instruction. For validation assays, total RNA was extracted using Trizol reagent (Invitrogen) according to the manufacturer's instructions. 1 μg of total RNA was retro-transcribed with oligo-dT oligonucleotides, using M-MLV reverse transcriptase (Promega). 15 ng of cDNA was used as template for PCR (GoTaq, Promega) and reactions were analyzed on agarose or acrylamide gels. Quantitative real-time PCRs (qPCR) were performed using LightCycler 480 SYBR Green I Master and the LightCycler 480 System (Roche), according to the manufacturer's instructions. Control reactions omitting M-MLV reverse transcriptase were also carried out. Oligonucleotides used are listed in Table S5.

RNA-sequencing Analysis

mRNA was processed according to Illumina TruSeq Stranded mRNA sample preparation protocol using 2,500 ng per sample. Samples were paired-end sequenced at the Donnelly Sequencing Centre (University of Toronto) on Illumina NextSeq500 using high-output v2.0 300c chemistry. All RNA-seq datasets were paired-end, 151-nucleotide length reads with 3 replicates for each sample. Read depth was at least 53M reads (GEO accession number GSE133711). All fastq files were initially quality checked and processed using FastqC (Wingett and Andrews, 2018) and Trimmomatics (Bolger et al., 2014) respectively. Transcriptome-wide AS and gene expression profiling were performed using the splicing and gene expression quantification tool "VAST-TOOLS" using the previously described workflow (Tapial et al., 2017). To comprehensively detect and quantify all AS events involving alternative exons, we used the VAST-TOOLS multi-module analysis pipeline, as previously described (Irimia et al., 2014). Briefly, reads were initially mapped to genome assemblies using Bowtie, using –m 1 –c 2 parameters with reads that mapped to the genome discarded for AS quantifications. Unique EEJ (exon-exon junction) libraries were generated to derive measurements of exon inclusion levels using the metric "Percent Spliced In" (PSI). This utilized all hypothetically possible EEJ combinations from annotated and *de novo* splice sites, including cassette, mutually exclusive, and microexon events (Irimia et al., 2014). Differential identification of PSI for AS events or percentage intron retained (PIR) for IR events were calculated using the Diff module (available at https://github.com/vastgroup/vast-tools). with a cutoff of 10PSI/PIR (Weatheritt et al., 2016). Briefly, diff is a differential splicing analysis module that uses Bayesian inference, where the prior distribution is a uniform Beta ($\alpha = 1$, $\beta = 1$), and the likelihood function follows a Binomial distribution where the number of inclusion reads K $\sim$Binomial (Ψ, N), where Ψ represents PSI or PIR, and N the total number of junction reads per-event. Following Bayes theorem we are left with a conjugate posterior distribution over $\Psi \sim$Beta (K + α, (N-K) + β). When replicates are available joint posterior distributions for a sample are estimated from sampling empirical posterior distributions of the replicates and fitting a new posterior Beta using maximum-likelihood (MLE) estimation in R. Statistical significance between two posterior distributions X $\sim$Beta, and Y $\sim$Beta, is calculated as P(X-Y > 0) and estimated using empirical distributions sampled from X and Y. Vast-tools diff analysis was also supplemented by vast-tools compare analysis. VAST-TOOLS is freely available via its github portal (https://github.com/vastgroup)." Clustering was done using the algorithm self-organizing maps and plots using R. Differentially expressed genes were identified using Deseq2 (Love et al., 2014) with an adjusted cut-off of 0.05, an absolute log fold change of > 1 required and a minimal expression level of 3 cRPKM.

Functional Enrichment Analysis

Ensembl gene ID for the gene expression and AS events regulated during the development of the cerebellum were uploaded to G:Profiler to perform functional enrichment analysis (https://biit.cs.ut.ee/gprofiler_archive2/r1760_e93_eg40/web/; Reimand et al., 2016), using a stringent background consisting of 12894 genes with the expression of at least cRPKM > 2 in one of the cerebellar samples. Benjamini-Hochberg FDR correction of hypergeometric test was applied. Analysis for enriched GO functional clusters was performed also in ENRICHR (http://amp.pharm.mssm.edu/Enrichr; Kuleshov et al., 2016). In this analysis, for the enriched terms highlighted, we indicated the ''combined score'' (the p value computed using the Fisher's exact test multiplied with the z-score of the deviation from the expected rank as follows: c = log(p) x z.

The list of candidate ASD susceptibility genes was obtained from the Simons Foundation Autism Research Initiative (SFARI) autism gene database (https://gene.sfari.org/) (Basu et al., 2009). The lists of genes associated with bipolar disorder and schizophrenia was obtained from the BDgene database (http://bdgene.psych.ac.cn) (Chang et al., 2013).

Laser-Capture Microdissection

Cerebella were obtained from P10 male mice, included in OCT compound (VWR), frozen in powdered dry ice and stored at −80°C. 10 μm frozen sections cut on a cryostat (Leica CM1850) were mounted on PET-membrane 1,4 μm frame slides (Leica) previously cleaned with RNase away (Molecular Bio Products) and UV-treated for 45 min under sterile hood. Modified Cresyl Violet staining for RNA research (0.5 g Cresyl violet into 50 mL 100% ethanol) was performed to visualize the neural structure. Approximately 800 μm2 of area for external granular layer (EGL) and 1210 μm2 for internal granular layer (IGL) from 9 mice were microdissected with a laser-microdissection system (Leica LMD6) and recovered in RNA later reagent (QIAGEN). Total RNA was extracted from the dissected specimen using a RNAeasy Micro Kit (QIAGEN) and quantified with Agilent Bioanalyzer 2100 using RNA600 picoKit. cDNA was reverse transcribed using SuperScript-IV VILO master Mix with EZ DNase (Invitrogen).

Binding Motif Enrichment Analysis

Sequence analysis for enriched motifs in developmental-regulated cassette exons was performed using computational tool available on the rMAPS web server (http://rmaps.cecsresearch.org/; Park et al., 2016). Exons belonging to different temporal clusters were compared to control exons (non-regulated, alternative exons). Alternative exons without splicing changes (< Δ10 PSI) in genes showing regulated AS during cerebellar differentiation were treated as control. Analysis were carried out using rMAPS default setting: 250 bp upstream or downstream intronic sequences and the first 50 bp of the 5′ or 3′ end of exonic sequences were scanned for motif occurrences. For intronic sequences, 20 bp sequence within the 3′ splice site and the 6 bp sequence within the 5′ splice site were excluded. Motif density was calculated by examination of a 50 bp sliding window, slided by 1 bp at a time. Wilcoxon's rank sum test was performed to identify motifs significantly enriched in specific position between regulated and control exons.

For splicing feature analysis, MaxEntScan (Yeo and Burge, 2004) was used to estimate the strength of 3′ and 5′ splice sites. 5′ splice site strength was assessed using a sequence including 3nt of the exon and 6nt of the adjacent intron. 3′ splice site strength was assessed using a sequence including −20nt of the flanking intron and 3nt of the exon. SVM-BPfinder (Corvelo et al., 2010) was used to estimate branchpoint and polyprimidine tract strength and other statistics. Score were estimated using the sequence of introns to the 3′end of exon between 20-500nt.

Protein Extracts and Western Blot analysis

P10 cerebella from *WT* and *Sam68*^{KO} male littermates were homogenized in RIPA buffer [50 mM Tris pH 7.4; 1% NP-40; 0.5% Na deoxycholate; 0.1% SDS; 150 mM NaCl; 1 mM EDTA; 1 mM DTT; 0,5 mM NaVO3; protease inhibitor cocktail (Sigma Aldrich)]. Lysates were incubated on ice for 20 min, briefly sonicated, and centrifuged (20 min at 12000*g*, 4°C). Protein extracts were quantified by Bradford assays and analyzed by Western Blot using the following primary antibodies: rabbit anti-Sam68 (dilution 1:2000, Bethyl), anti-GRIA2 (dilution 1:1000, Immunological Science) and anti-U2AF65 (dilution 1:500, Sigma-Aldrich), mouse anti-ACTIN (dilution 1:1000, Santa Cruz). Anti-rabbit, anti-mouse (GE Healthcare) HRP-link

ed secondary antibodies were used at 1:10000 dilution and ECL signal developed using Clarity Western ECL Blotting Substrate (Biorad).

Crosslinking-Immunoprecipitation Experiment

The CLIP assay was performed as previously described (Bielli and Sette, 2017). Briefly, cerebella from P10 *WT* and *Sam68*^{KO} male littermates were minced mechanically in PBS, UV-irradiated (400 mJ/cm2) and collected in lysis buffer [50 mM Tris pH 8.0, 100 mM NaCl, 1 mM MgCl2, 0.1 mM CaCl2, 1% NP40, 0.1% SDS, 0.5 mM Na3VO4, protease inhibitor cocktail (Sigma-Aldrich), RNase inhibitor (Promega)]. Samples were briefly sonicated and incubated with DNase (RNase-free; Ambion) for 15 min at 37°C and then centrifuged at 15000 g for 5 min at 4°C. For input RNA, 10% of extract used for immunoprecipitation was treated with Proteinase K for 1 h at 55°C and RNA was purified by standard procedure. For immunoprecipitation, 0.3 mg of extract was diluted to 1 mL with lysis buffer and incubated with anti-Sam68 (Bethyl), anti-U2AF65 (Sigma Aldrich) antibodies or IgGs (negative control) in the presence of protein G magnetic Dynabeads (Novox; Life Technologies). 10 μl/ml of RNase I 1:1000 (Ambion) was added and reactions were incubated for 2 hr at 4°C under rotation. After two washes with high-salt buffer (50 mM Tris–HCl, pH 7.4, 1 M NaCl, 1 mM EDTA, 1% Igepal CA-630, 0.1% SDS, 0.5% sodium deoxycholate) and Proteinase K buffer (100 mM Tris–HCl, pH 7.4, 50 mM NaCl,

10 mM EDTA), an aliquot (10%) was kept as a control of immunoprecipitation, while the rest was treated with 50 μg Proteinase K and incubated for 1 h at 55°C. RNA was then isolated by standard procedures. All oligonucleotides used for qPCR analyses are listed in Table S5.

RNA pull-down

Sam68-regulated exons in *Arhgap12* and *Arhgef9* and ~250-300 nucleotides of the upstream intronic region were amplified from mouse genomic DNA with the primer sequences given in the Table S5. PCR products were cloned into the *Mfe*1 site in pXJ41 (Ehrmann et al., 2016). Biotin-RNA pull-down experiments were performed using HEK293T nuclear extracts and *Arhgef9* or *Arhgap12* RNA probes synthesized *in vitro* from a PCR product amplified using primers indicated in the Table S5 in the presence of biotin-labeled deoxynucleotide (Roche), as previously described (Pagliarini et al., 2015). Extracts were precleared for 1 hr on protein A–Sepharose beads (Sigma-Aldrich) and 1 hr on streptavidin-Sepharose beads (Sigma-Aldrich). Precleared extracts were then incubated with streptavidin-Sepharose beads in the presence of 0.1% BSA and biotinylated RNA probe for 2 hr at 4°C under rotation. Beads were washed three times and proteins were eluted in SDS sample buffer for western blot analysis (Pagliarini et al., 2015).

Histology, immunohistochemistry and colocalization analysis

Age-matched brains from *WT* and *Sam68*^{KO} male littermates were dissected, fixed in neutral buffered 10% Formalin solution (Sigma-Aldrich), dehydrated, and embedded in paraffin for microtome serial sectioning (8-10 μm thickness). De-paraffined mid-vermal sagittal sections were stained with hematoxylin and eosin (H&E, Sigma-Aldrich) or processed for immunofluorescence labeling and 4', 6-diamidino-2-phenylindole (DAPI; Thermo Fisher Scientific, Waltham, MA, USA) staining, according to standard protocols with antigen retrieval. Fluorescence and bright-field micrographs were acquired with a motorized LMD7000 microscope or with TCS SP5 laser scanning confocal microscope (Leica Microsystems). For quantification of cerebellar layer thickness of P10 pups, three images (at identical locations in the cerebellar vermis, in lobules VI, VII and VIII) from 3 different animals of each genotype group were analyzed with Imaris Software (Bitplane, Zurich, Switzerland). Colocalization analysis was performed using the ''Colocalization threshold'' plugin of ImageJ (FiJi) software. Colocalization of VGLUT1 and CALB was evaluated by Pearson's Correlation Coefficient (PCC). For each multichannel acquired image, the analysis was performed on a manually selected region of interest (ROI) in the proximal branches of PC dendrites. More than 20 ROI per animal in at least 3 animals per genotype were analyzed.

BrdU incorporation

P10 *Sam68*^{KO} and wild-type male littermates received a single BrdU injection (0.1 mg/g body weight) 2 h prior to euthanasia. Brains were dissected and tissue preparation and processing was performed as described in M&M. Double immunofluorescence labeling was performed using anti-BrdU antibodies. Fluorescence micrographs were acquired with a motorized LMD7000 microscope (Leica Microsystems) using the manufacturer's imaging software. BrdU-labeled cells in EGL were quantified with the ImageJ analysis software. Sections of similar size in similar regions were chosen and analyzed. The average count of positive cells was obtained from 3 non-adjacent sections from each animal (n = 3) and plotted as the mean number of positive cells over layer length. All measurements were performed with the observer blind to the identity of the slides.

Antibodies Used for Immunofluorescence Labeling

5-bromo-2′-deoxyuridine (BrdU): Millipore monoclonal antibody, clone BU-1, 1:100; Calbindin 1 (CALB1/CALBD-28K; 1:200, clone CB-955, Sigma- Aldrich); vesicular glutamate transporter 1 (VGLUT1; 1:1000, Synaptic System).

Electrophysiology

WT and *Sam68*^{KO} male littermates were killed by cervical dislocation, and cerebellar parasagittal slices (210 μm) were prepared from fresh tissue blocks of the brain using a vibratome. After 1 hr of recovery time in a chamber containing oxygenated artificial cerebrospinal fluid (ACSF), single slices were transferred to a recording chamber and submerged in a continuously flowing ACSF at 2–3 ml/min gassed with 95% O2%–5% CO2. The composition of the ACSF was: 126 mM NaCl, 2.5 mM KCl, 1.2 mM MgCl2, 1.2 mM NaH2PO4, 2.4 mM CaCl2, 11 mM glucose, and 25 mM NaHCO3. Purkinje cells (PCs) could be identified using an Olympus BX50WI upright microscope with a × 40 water-immersion objective combined with an infrared filter. Whole-cell patch-clamp recordings were made in voltage-clamp mode at the holding potential of − 70 mV with borosilicate glass pipettes (1.8 mm outer diameter; 2–4 MΩ) pulled with a horizontal micropipette puller (Sutter Instrument). The recording pipettes were filled with internal solution containing the following: 125mM K+-gluconate, 10 mM NaCl, 1mM CaCl2, 2mM MgCl2, 0.5mM BAPTA, 10mM HEPES, 0.3mM GTP, 3mM Mg-ATP, adjusted to pH 7.3. Series resistance was usually comprised between 10 and 20 MΩ. PCs were identified also immediately after rupture of the GΩ seal, by evaluating their firing response to the injection of depolarizing current. Spontaneous synaptic events were stored using P-CLAMP 10 (Molecular Devices) and analyzed offline on a personal computer with Mini Analysis Version 6.0.7 software (Synaptosoft). To detect spontaneous excitatory postsynaptic currents (sEPSCs), Bicuculline (10 μM) was added to the external solution to block GABA-mediated transmission and mEPSC were recorded in the presence of the voltage-gated sodium channel blocker tetrodotoxin (TTX, 1μM). The detection threshold of spontaneous and miniature excitatory events was set at twice the baseline noise. Positive events were confirmed by visual inspection for each experiment. The fact that no false events would be identified was confirmed by visual inspection for each experiment. Offline analysis was performed on synaptic events recorded

during fixed time epochs (1 min). Only PCs with resting potential in a range of 50-60 mV, were taken into account. One to five cells per animal were recorded. For electrophysiological experiments ''n'' refers to the number of cells.

CatWalk Test

The gait of mice was performed in a darkened room with red light and sheltered from noise by using the CatWalk XT 8.1 system (Noldus Information Technology, Wageningen, Netherlands) (Vandeputte et al., 2010). This apparatus consisted of a 1.3 m black corridor led over a glass plate that was illuminated by a green LED light. As soon as the mouse's paw touched the glass slide, this green light was reflected and a high-speed camera underneath the glass could then capture the resulting illuminated green footprint. The mice must cross the walkway from the start to their cage. A trial was regarded as compliant by the software if the animal did not show a maximum speed variation greater than 60%. All trials marked by the software as compliant were reviewed manually: if the animal stopped or turned in mid-run the trials were not included in the analysis. Five compliant runs were recorded for each mouse and the resulting data automatically analyzed by the CatWalk XT software according pre-set paradigms.

Social approach and social novelty preference assay

Subject animals were handled by the operator prior to behavioral tests and acclimated for at least 30 min in the behavioral room. All behavioral tests were conducted between 10:00am and 3:00pm and were video recordered while the experimenter was monitoring in blind the trials from a separate room behavioral analyses was done blind, which is critical.

The three-chamber social-behavior test was performed as previously described (Moy et al., 2004), with small modifications. The apparatus consisted of a plastic box divided into 3 chambers (length: 70 cm; width: 50 cm; and height: 50 cm). Male *WT* or *Sam68*^{KO} mice littermates at P45 were first placed in the middle chamber with the doors opened and left free to move for 10 min (habituation phase). After habituation, on the two lateral chambers, two chrome wired cages were placed that contained on the left, an unfamiliar mouse ''Animal'' (age matched *WT* C57BL/6J male mouse) and on the right, an object, with the experimental mouse free to move for 10 min (Phase 1). At the end of Phase1, subjects were returned to the middle chamber with no access to other chamber. A second, unfamiliar mouse (''Novel Animal''; age matched *WT* C57BL/6J male mouse) was placed in the chamber that had the object during Phase1 while the ''Animal'' remained in the same chamber as ''Familiar Animal.'' Each subject mouse was then tested in a second 10-min session to assay social preference for the new animal (Phase 2). The movements of the test mice were recorded using a digital video camera placed on top of the cage and tracked using the Ethovision XT software. The distance traveled and the time that the mice spent exploring the left and right chambers during the habituation phase of the test were quantified to evaluate the exploratory ability and the absence of spontaneous preference for the left versus the right side. The time of direct interaction was quantified evaluating the time spent sniffing the cage with object or the stranger mouse (Phase1) or sniffing the cage with familiar or new mouse (Phase 2).

Olfactory tests

The buried test was performed as indicated in Yang and Crawley (2009). Briefly, three days before the test, a cookie was placed in the cage of the test mice overnight to evaluate the palatability of the new food. The evening before the test, the normal food was removed by the cage. On the day of the test, P60 male *WT* or *Sam68*^{KO} littermates were placed in a new cage containing three cm deep bedding and allowed to explore for 10 min. The animal was removed from the cage and the cookie was buried ~1 cm beneath the surface in a random corner of the cage. After returning the mice back in the cage, time of latency to find the cookie were measured in a 15-min period.

The habituation/dishabituation test as indicated in Yang and Crawley (2009), with small modifications. Adult (P60) male *WT* or *Sam68*^{KO} littermates mice were allowed to habituate for 30 min to a new clean cage in which a dry cotton-tipped wooden applicator was inserted. 50 μL of water or urine was added to the applicator and the odors was presented in three consecutive trials of 2 min each with an interval of 1 min. Sniffing time was recorded when the animal was oriented toward the cotton tip with its nose within 2 cm of the tip. The male and female (asynchronous for estrous cycle) urine from multiple adult mice was collected.

QUANTIFICATION AND STATISTICAL ANALYSIS

Data are presented as mean ± SEM unless otherwise indicated. All tests were performed using GraphPad Prism6. $p < 0.05$ was considered significant. The machine learning algorithm analysis self-organizing maps was undertaken using the ''som'' R package with topol = 'hexa',neigh = 'Gaussian'. For gene function enrichment analysis, significance was assessed using the hypergeometric test with multiple testing correction using the method of Benjamini and Hochberg. Fisher's exact test was used for comparing count data and the Wilcoxon rank-sum test was used for comparing distributions. Background datasets for both AS events and genes calculated using only AS events ($0.05 < PSI < 0.95$) or genes (cRPKM > 3) across all datasets. Vast-tools diff analysis uses Bayesian inference with a beta distribution, and joint posterior distributions for a sample were estimated from empirical posterior distributions of the replicates using maximum-likelihood (MLE) fitting.